Observation of Bragg-Type Ocean Doppler Spectra with the TIGER SuperDARN Radar

A thesis presented by

Robert Greenwood

In partial fulfilment
of the requirements for the degree

Bachelor of Space Science (Honours)

In the subject of

Physics

Department of Physics
School of Engineering and
Mathematical Sciences
La Trobe University
Bundoora, Victoria
November, 2004

Observation of Bragg-Type Ocean Doppler Spectra with the TIGER SuperDARN Radar

A thesis presented by

Robert Greenwood

In partial fulfilment
of the requirements for the degree

Bachelor of Space Science (Honours)

In the subject of

Physics

Department of Physics
School of Engineering and
Mathematical Sciences
La Trobe University
Bundoora, Victoria
November, 2004

Contents

Abstract

Large military Over-The-Horizon Radars can measure ocean wave heights, surface currents, and surface wind directions over vast, remote regions. It has long been a dream to deploy a network of relatively compact, portable sky-wave radars dedicated to the provision of real-time oceanographic and meteorological data. I demonstrated the potential for the SuperDARN radars to achieve this. This has become possible with the implementation of a new radar operating system which permits the acquisition of complex time series data. In this project it has been shown that SuperDARN radars and TIGER specifically are capable of deducing relevant sea state properties. Radio waves are backscattered from ocean waves in a way completely analogous to Bragg scatter of X-rays from crystals. That is, constructive interference of the backscattered signal occurs for ocean waves equal to half the transmitted radio wavelength. FITACF has been able to detect sea scatter, but due to the high relative errors for low Doppler velocities, sea state information cannot be obtained by this type of analysis. The application of Dr. Sessai Yukimatu's raw time series operating system allowed a more rapid sampling rate whilst still avoiding range aliasing ambiguities. The in-phase and quadrature amplitudes were averaged to form evenly spaced time series, and then Doppler spectra were obtained by applying a Fourier transform. The resulting Doppler spectra exhibited the idealised form expected for sea scatter. From these spectra, prevailing wind-wave directions could be estimated by comparing the ratio of the Bragg peak amplitudes to a model of the directional sea spectrum.

Statement of Authorship

Except where reference is made in the text of the thesis, this thesis contains no material published elsewhere or extracted in whole or in part from a thesis submitted for the award of any another degree or diploma.

No other person's work has been used without due acknowledgement in the main text of the thesis.

The thesis has not been submitted for the award of any degree or diploma in any other tertiary institution.

Robert Greenwood

Acknowledgements

I would like to thank Dr. Murray Parkinson, for without his ever present near omni wise advice; this project would never have got off the ground.

Thank you also Professor Peter Dyson. You gave me a lot of helpful, insightful advice during the course of this project.

Thank you Dr. Harvey Ye for taking the time to install the new software and get it working.

Thank you Dr. Sessai Yukimatu for without your intellectual property I would not have had a project.

Thank you to Professor Mark Lester who was always busy, but always made time to answer my questions.

Thank you to all the 4th Year Students who have been great vessels for bouncing ideas around, and who have offered valuable practical advice.

Lastly, but most of all, I would like to thank my gorgeous fiancée Courtney, for all her support and understanding thought the year.

1 Physical and Radar Oceanography

1.1 Theory of wind-wave generation and propagation

Most ocean waves are produced by surface wind. As the wind blows over vast expanses of water, it interacts through friction with the surface of the water. First, small ripples are created as local instabilities are formed by one water molecule moving on top of another, and then falling due to gravity. These ripples become larger as the wind pushes more water up the back; the waves steadily increase in size. Buoyancy forces also help to maintain the waves. The process of increasing wave size continues until an equilibrium is achieved. Figure 1.1 shows the water particle motion for surface gravity waves in deep water.
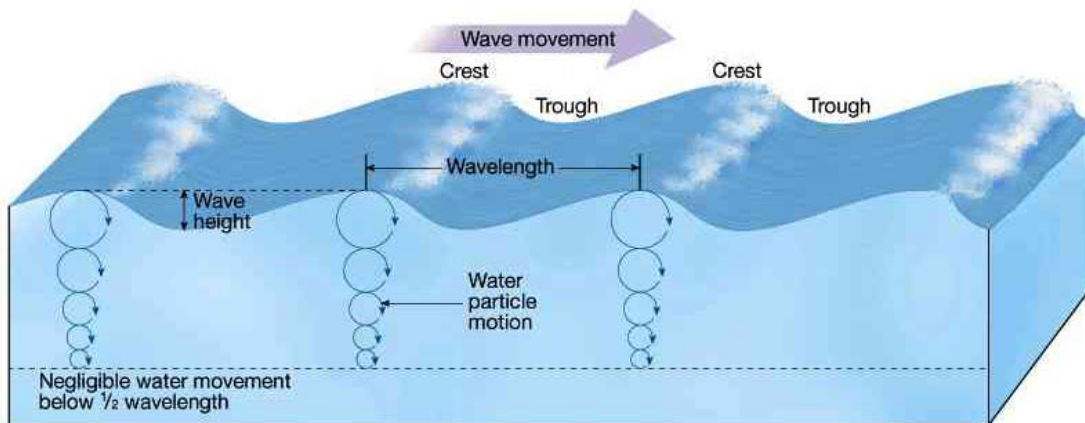
Figure 1.1: Diagram showing wave motion for gravity waves in deep-water [Courtesy of the University of Victoria].

The frequency of the waves, f, and the wave length of the waves, L_n, are related by the gravity wave dispersion relationship [1] [2]:

$$\omega^2 = gk \tanh(kd) \tag{1.1}$$

where ω is the wave frequency in radians per second and is related to f by $\omega = 2\pi f$. Other parameters include g, the acceleration due to gravity, d, the water depth and k, the wave number. The latter is related to the wave length of the waves by:

$$k = \frac{2\pi}{L_n} \tag{1.2}$$

In the case of deep water, d is very large with respect to L_n, and as a result $kd \gg 1$, and tanh $(kd) = 1$. This simplifies equation (1.1) to:

$$\omega^2 = gk \tag{1.3}$$

Equation (1.3) is known as the deep-water dispersion relation. The phase velocity, v_n, is the speed at which a surface wave of a specific wavelength propagates at, and is given by the relationship:

$$v_n = \frac{\omega}{k} \tag{1.4}$$

Substituting equation (1.2) and (1.4) into equation (1.3) gives:

$$v_n = \sqrt{\frac{gL_n}{2\pi}} \tag{1.5}$$

This shows that all waves of a particular wavelength move with the same velocity. Therefore, the phase velocity of a wave observed by a backscatter radar is dependent on the frequency transmitted by the radar.

For a wind that has been blowing for several days with roughly constant velocity over a region of deep water unlimited in fetch, a wave spectrum will be produced. Figure 2.2 shows measured wave spectra for a fully developed sea for different wind speeds.
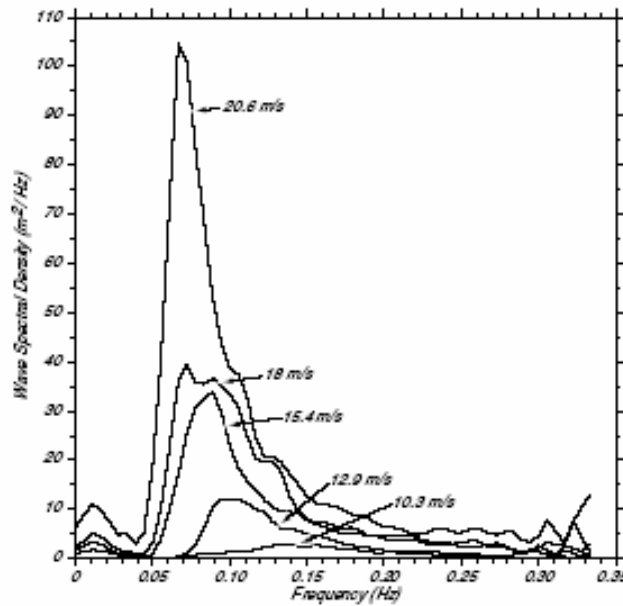

Figure 2.2: Wave spectra of a fully developed sea for different wind speeds [3] [2]

In a fully developed sea there is a dominant peak at a preferred wavelength for a given wind speed. By analytical means, the following equations were found to be a good fit to the measurements shown in Figure 2.2 [2]:

$$S(\omega) = \frac{\alpha g^2}{\omega^5} \exp\left[-\beta \left(\frac{\omega_0}{\omega} \right)^4 \right] \qquad (1.6)$$

where $\alpha = 8.1 \times 10^{-3}$, $\beta = 0.74$, $\omega_0 = g\,/\,U_{19.5}$ and $U_{19.5}$ is the wind speed at a height of 19.5 m above the sea surface. This model is known as the Pierson-Moskowitz spectrum

Solving dS / dω = 0 gives:

$$\omega_p = \frac{0.877 g}{U_{19.5}} \qquad (1.7)$$

where ω_p is the frequency of the peak wave spectral density. This result allows estimation of the surface winds over regions of open ocean by measuring the wind-wave spectrum.

Waves do not only travel in the direction of the prevailing wind; they travel in all directions, but with a peak of the distribution in the prevailing wind direction. The distribution of directions is called a directional wave spectrum. A simple but reasonable model for the directional wave spectrum will be presented in Chapter 3.2.1.

1.2   Experimental techniques for measuring sea state

The ocean has been a subject of interest ever since mankind set eye on the ocean. This interest has not waned over the years, as more structures are being built on, in, or near the ocean. It is important to know the conditions that one might encounter in specific regions. For example, probable wave sizes are an important consideration when building oil rigs in the open sea. Other information can also be determined from ocean waves, such as wind direction and speed. This information can be used to help drive atmospheric models. In this regard, many techniques have been developed for measuring sea state.

By far the earliest method is direct human observation. Before the advent of wave buoys, radars, satellites and other autonomous devices, the only way of measuring sea

state was by looking and taking notes. Quite obviously, this type of measurement lacks the quantitative reliability of modern, digital signal processing techniques. However it does have the advantage that no equipment other then pen and paper is needed (or these days a laptop).

A modern approach involves the use of buoys to house devices that can measure specific phenomenon at specific locations, both autonomously and continuously. An important example of these is the accelerometer, which basically measures the acceleration imparted on the wave buoy. This allows the collection of wave heights and wave frequency [4]. The wave heights can be calculated by calculating the double integral to give position; basically, the difference between the maximum and minimum positions gives the wave height. The wave frequency can be determined by the time taken for the wave to go from a minimum height to a maximum height. Wave buoys have the advantage of providing low cost, continuous and reliable data over coastal regions. However, this type of measurement is confined to coastal regions free of shipping lanes. The maximum depth a wave buoy can be placed in is 1.7 km [courtesy of Civil Tek, Inc.], and deployment of a buoy in the open ocean is obviously fraught with difficulties.

The use of devices on satellites is another approach to the measurement of sea state. Synthetic aperture radar (SAR) and wind scatterometers both use microwave signals to probe the ocean surface. Using accurate measurements of the radar backscatter signal, SARs can detect information about the surface feature and further analysis provides information about the wave spectrum. Wind scatterometers have a narrow spectral bandwidth which can resolve the surface ripples and their orientation with respect to the satellite motion. This enables the derivation of surface wind speeds and direction [courtesy of the Committee on Earth Observation Satellites]. Radar altimetry can be used to measure the height profile of the ocean under the path of the satellite, providing information about significant wave heights. Meteorological satellites can also measure atmospheric wind speeds by tracking clouds. There are a lot of advantages to using satellites, the main being that they provide information over a very large region, and often over remote regions that would otherwise not be observed. However, satellites are very expensive and once they are in place it is

difficult to maintain and upgrade them. Also, the same region can only be sampled once per orbit at the very best.

Both surface wave and over-the-horizon radars (OTHR) operating at MF, HF and VHF can be used to measure sea state. The basics principles are the same for the different kinds of radar: they interact with the ocean waves that have a wavelength equal to half the radio wavelength (i.e., Bragg scattering). Information about wavelengths, wave heights, the scalar and directional wave spectra, surface currents, wind directions, and wind speeds can be measured. The advantage of HF radars is that they cover a large region of ocean, especially OTHRs, and can do so at a fraction of the cost of most satellites. The powerful military HF radars are best equipped to study the ocean, but are dedicated to the detection of both military and illegal shipping and aircraft. Although the SuperDARN network of OTHRs is dedicated to the study of the ionosphere, they offer the hope of providing low cost, continuous measurement of sea state across vast remote regions.

A summary of the pros and cons of various methods is summarised in Table 1.1.

Table 1.1: Summary of the advantages and disadvantages of various experimental techniques

Experimental technique	Advantages	Disadvantages
Observers	• Continuity with historical records • Active interpretation	• High cost • Limited coverage
Buoys	• Autonomous collection • Low costs • Quantitative	• Limited coverage • Must be anchored
Satellites	• Large coverage • High resolution	• Expensive • Extremely Isolated
HF Radars	• Large coverage • High resolution • Moderate cost	• Ionospheric effects • Large real estate • Have other priorities

1.3   Radar oceanography

Large military OTHRs such as the Jindalee Skywave radar [5] and the American OTHRs used by the Environmental Technology Laboratory (ETL) [6] of the National Oceanic and Atmospheric Administrations (NOAA) have shown that sea state can be measured by OTHRs. The aim of this project is to demonstrate that SuperDARN (see Chapter 2.1.1) OTHRs can also be used to investigate ocean-wave parameters as a zero cost by-product of routine ionospheric research. This has never been attempted before.

There are two main types of radar that appear in the literature: surface wave mode current mapping radars [7] [8] [9] and the aforementioned military OTHRs. Surface wave radars are usually smaller systems dedicated to coastal monitoring. They rely on the radio waves refracting across the surface of the ocean, and are limited in range to ~100 to 400 km. The range is much less than that of OTHR, but problems that arise from interference from the ionosphere are reduced.

The basic principle that allows both kinds of radars to study ocean waves is entirely analogous to Bragg scatter of X-rays from crystals. Figure 1.3 shows the geometry of waves scattering off a regular lattice. Ocean waves appear as a regular lattice to HF radio waves, and can be understood in the same way.
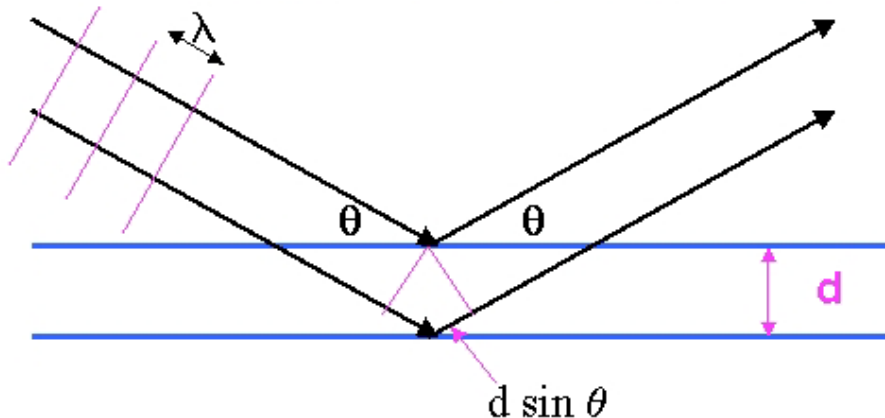

Figure 1.3: Geometry of rays reflected from a regular lattice.

For constructive interference to occur:

$$2d\sin(\theta) = n\lambda \tag{1.8}$$

where d is the lattice spacing, λ is the radio wavelength, θ is the angle of incidence and n is some integer greater than zero. A monostatic radar will preferentially observe rays that are directly backscattered from the sea. That is, $\theta = 90°$. To the first order, this gives the relationship:

$$\lambda = 2d \qquad\qquad (1.9)$$

Relating this to radar oceanography; λ is the wavelength of the transmitted pulse and d is the wavelength of the waves. Information gathered in this way can be used to determine many aspects of sea state including dominate wave and wind direction. The wind speed can be estimated from the second order backscatter spectrum (an account of this theory is beyond the scope of this pilot study). A detailed account of how to determine wind-wave parameters is given in Chapter 3.2.1.

2 SuperDARN, TIGER and HF radio wave propagation

2.1 SuperDARN radars and TIGER

2.1.1 Super Dual Auroral Radar Network (SuperDARN)

The Super Dual Auroral Radar Network (SuperDARN) consists of 15 radars supported by 11 countries. Figure 2.1a shows the fields of view for the 9 northern hemisphere radars, and Figure 2.1b shows the fields of view for the 6 southern hemisphere radars. As can be seen, the radar network covers vast and remote regions of arctic and subarctic ocean critical to the regulation of global climate change. Unlike satellite-based instruments, HF radars permit continuous monitoring of these regions.
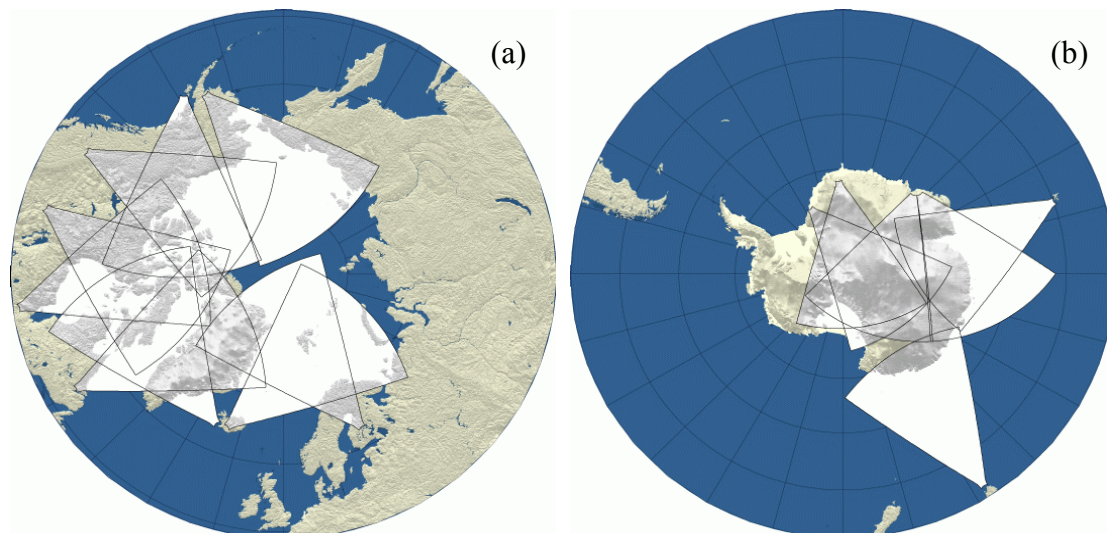

Figure 2.1: Fields of view of SuperDARN radars for (a) the Northern Hemisphere and (b) the Southern Hemisphere. The white areas delineate parts of the fields of view that cover sea and ice [courtesy of the SuperDARN website].

However, SuperDARN radars were designed to study magnetosphere-ionosphere coupling at high latitudes. They transmit HF radio waves with frequencies of 8–20 MHz, and corresponding wavelengths of 37.5–15 m. These HF waves interact with irregularities in the ionospheric plasma with a scale size of half the transmitted wavelength via Bragg backscatter. The same applies to backscatter from the ocean, namely the radars are sensitive to sea waves of length 18.75 m to 7.5 m. Being coherent systems, the radars measure the in-phase and quadrature components of the backscattered signals.

SuperDARN radars transmit a pulse set (Figure 2.2) that permits the calculation of complex auto correlation functions (ACFs). The radar operating system allocates less than 100 ms per pulse set, so for typical integration times of 7 s, the ACFs for approximately 70 pulse sets are coherently averaged. The resulting ACFs (e.g., Figure 2.3a) are then analysed by the FITACF algorithm [10] [11]. The arctangent of the ratio of the real and complex components of the ACFs gives the variation of phase, and
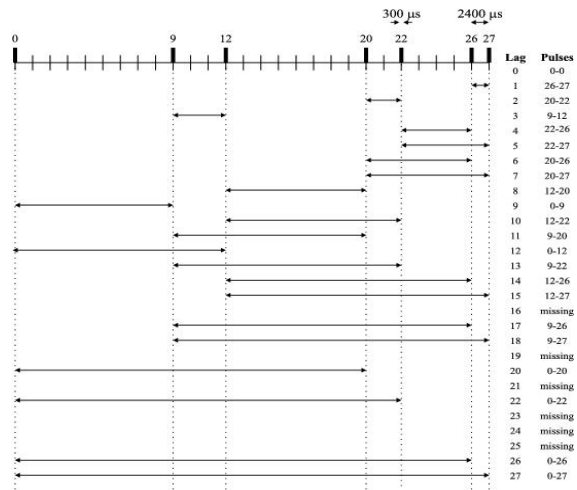

Figure 2.2: The 7-pulse sequence transmitted by the SuperDARN radars. The pulses are 300 μs long, and they are separated by integer multiples of the lag length, τ, which is normally set to 2400 μs. [courtesy of the University of Saskatchewan]

hence the line-of-sight Doppler velocity (Figure 2.3b). FITACF calculates many parameters, including the backscatter power, line-of-sight Doppler velocity and spectral width. FITACF also flags the scatter as either ionospheric or ground scatter.
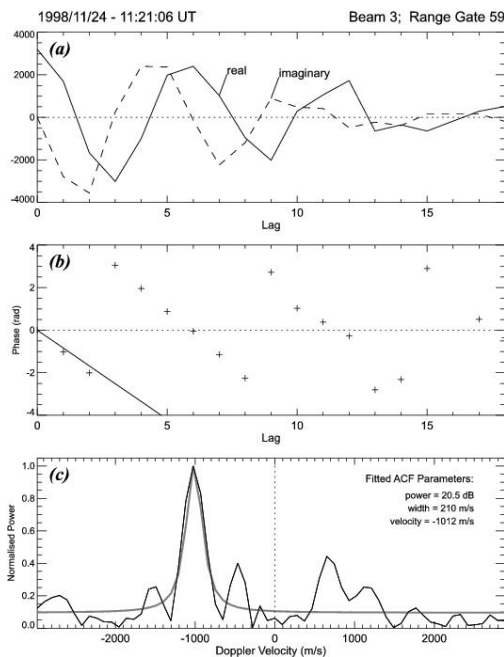

Basically, echoes with high Doppler velocity or high spectral width are identified as "ionospheric scatter," whereas regions with low Doppler velocity and low spectral width are identified as "ground scatter." Figure 2.3c shows a Fourier transform of the time series of the complex amplitudes of the ACF shown in part a. This transformation produces a Doppler spectrum for which line-of-sight velocities can also be determined via a different approach to that adopted by FITACF.

Figure 2.3: (a) The complex ACF measured along beam 3 at range gate 59 at 11:21:06 UT on 24 November 1998 by the þikkvybær SuperDARN radar, Iceland. (b) The phase of the ACF (crosses), which aliases at ±π, and the fitted phase (solid line) determined by FITACF. (c) The normalised power spectrum (black line) obtained from the Fourier transform of the ACF, and the model power spectrum calculated using the velocity, power and spectral width parameters determined by FITACF [courtesy of the University of Saskatchewan]

There are three kinds of operating times for SuperDARN radars, "Common Time," "Special Time," and "Discretionary Time." Common Time comprises at least 50% of the overall operating time available to the radar network. Features of the standard Common Time program are listed in Table 2.1. Special Time comprises a maximum of 20% of the available operating time, and involves the use of some or all SuperDARN radars. All radars that are involved will usually run the same operating mode to achieve a common goal.

Table 2.1: SuperDARN Common Time Program as per the SuperDARN Principle-Investigators agreement

- Full 16-beam azimuth scan by each radar
- Westerly radar of each pair scans clockwise
- Easterly radar of each pair scans counterclockwise
- Each scan commences on 2-minute boundary
- Integration time on each beam: 7 seconds
- Initial range sampled: 180 Kilometres
- Number of ranges sampled: 70
- Range separation: 45 Kilometres
- Transmitter pulse length: 300 microseconds
- Pulse pattern is the standard 7-pulse set
- Frequency is adjustable for best overlap in common viewing area

Discretionary Time comprises a maximum of 30% of the available operating time. The main distinction between Special Time and Discretionary Time is that for Discretionary Time only one radar or radar pair is used. Times not used that are allocated towards Special Time and Discretionary Time operations revert to Common Time operation.

2.1.2   The Tasman International Geospace Environment Radar (TIGER)

The Tasman International Geospace Environment Radar or "TIGER" is the acronym for a major project consisting of two radars. One of the radars is located on Bruny Island (43.38°S, 147.23°E) (Figure 2.4), off the South-East coast of Tasmania [12].

Figure 2.4: TIGER radar, located off the South-East coast of Tasmania (43.38°S, 147.23°E)

The other TIGER radar, TIGER Unwin, is under construction near Invercargill, New Zealand (46.51°S, 168.38°E). Its field of view will overlap the field of view of the TIGER Tasmania radar. Only data recorded with the Tasmanian radar was available for this study.

The main advantage of TIGER for ionospheric research is that it is located further equatorward than any other SuperDARN radar. From the point of view of this study, its field of view covers more ocean/sea than any other SuperDARN radar, including those in the Northern Hemisphere. This is illustrated in Figure 2.5, where the fields of view of the 6 Southern Hemisphere radars are shown. The shaded parts of the fields of view are those covering land. The red field of view corresponds to the TIGER Tasmania radar.
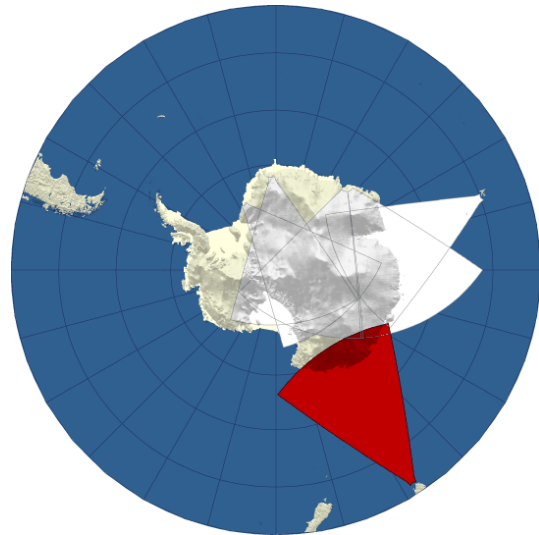

Figure 2.5: Fields of view of Southern SuperDARN radars, TIGER can be seen shaded red [courtesy of the SuperDARN website].

When completed, the TIGER Unwin (New Zealand) radar will provide an overlapping field of view. Statistically, the largest seas in the world are encountered in the TIGER field of view. This makes TIGER an ideal SuperDARN radar for oceanographic research.

2.1.3   TMS operating system

The "TMS" or raw time series analysis method of Dr. Sessai Yukimatu was initially developed to permit detection and measurement of individual meteor echoes by SuperDARN radars, and hence to obtain improved measurements of mesospheric winds [6]. The TMS approach was developed because the pulse set/FITACF technique lacks the temporal resolution required to resolve the true Doppler characteristics of short-lived meteor echoes. The standard mode of SuperDARN operation employs 7-second integrations, yet the typical duration of meteor echoes is

less than one second. Hence the rapid rise and slow decay of a meteor echo cannot be resolved. Failure to correctly identify and measure the Doppler characteristics of meteor echoes can result in large errors for the estimated neutral winds. The TMS approach circumvents this problem by extracting high time resolution in-phase and quadrature samples from the raw pulse set data.
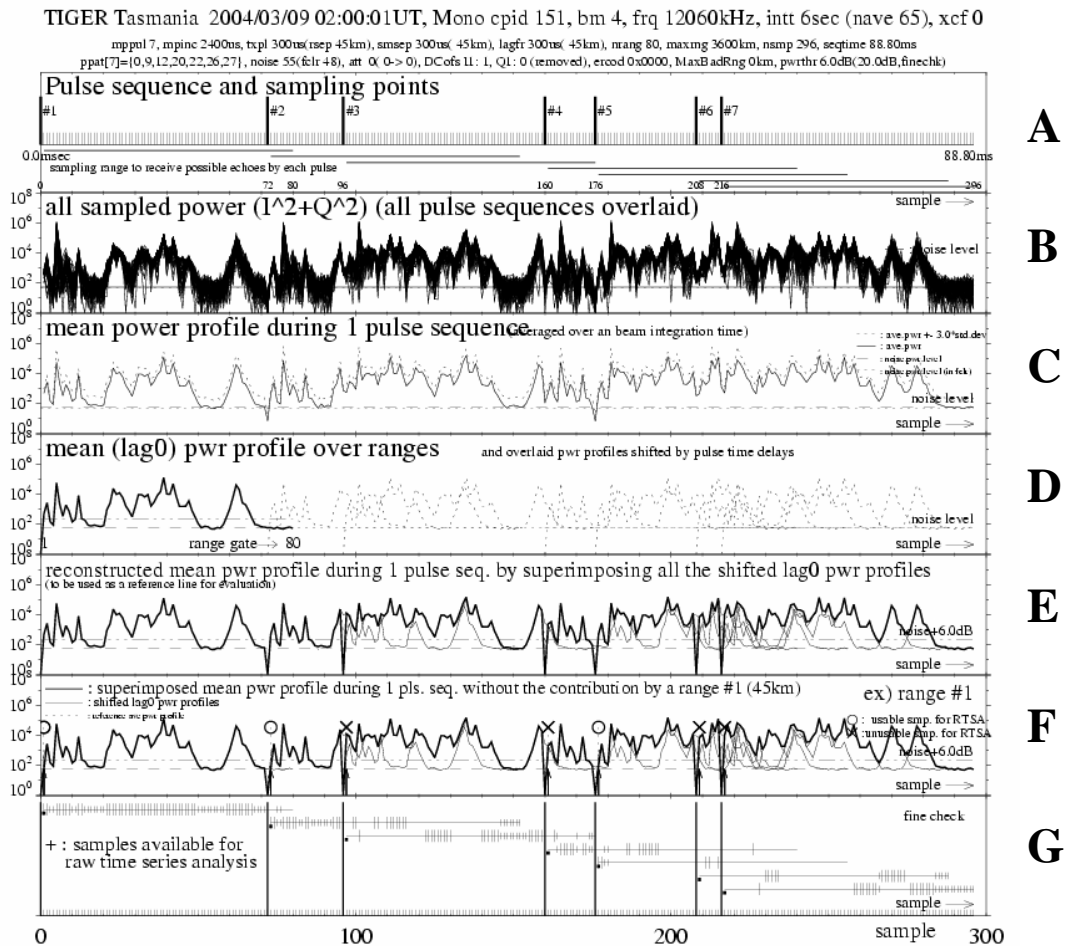

Figure 2.6: SuperDARN pulse sequence and the TMS analysis method [13]

The SuperDARN pulse set was designed to moderate the effects of range aliasing and the TMS approach builds upon this technique by rejecting aliased echoes, whilst at the same time achieving much higher time resolution. The TMS method is explained with the help of Figure 2.6. Part A shows the standard pulse set used by SuperDARN radars, as was seen in Figure 2.2. Part B is the power sampled by all pulse sets during an entire integration time (i.e., the results of 65 pulse sets). Part C is the mean power profile obtained by averaging the 65 curves superimposed in part B. Part D is the power for a single pulse averaged over the integration time. The power for this single pulse was obtained from the first pulse only, and represents the results that would be

17

obtained for every pulse if there were no range-aliasing. Part E is obtained by superimposing the single pulse set results shown in part D at the start of each pulse in the pulse set. If the effects of range-aliasing are reproduced the resultant curve should be completely equivalent to the mean power curve shown in part C. Part F compares part E with part C, subtracting samples whose powers are high in part E compared to those in part C as have having range-aliasing ambiguities. The circles and crosses identify the samples for range bin 4 that are usable and unusable for raw time series analysis, respectively. Part G summarises the usable results obtained in a similar way for all range bins. That is, the vertical dashes represent the usable samples for raw time series analysis. This method also monitors and removes SuperDARN radar DC offsets to permit reliable determination of echo amplitude and phase [14].

Figure 2.7 shows an example of meteor echoes detected by TIGER using the TMS operating system. This demonstrates the successful implementation of the new operating system on TIGER. The TMS operating system opens the door to many scientific applications, including the one explored in this thesis.
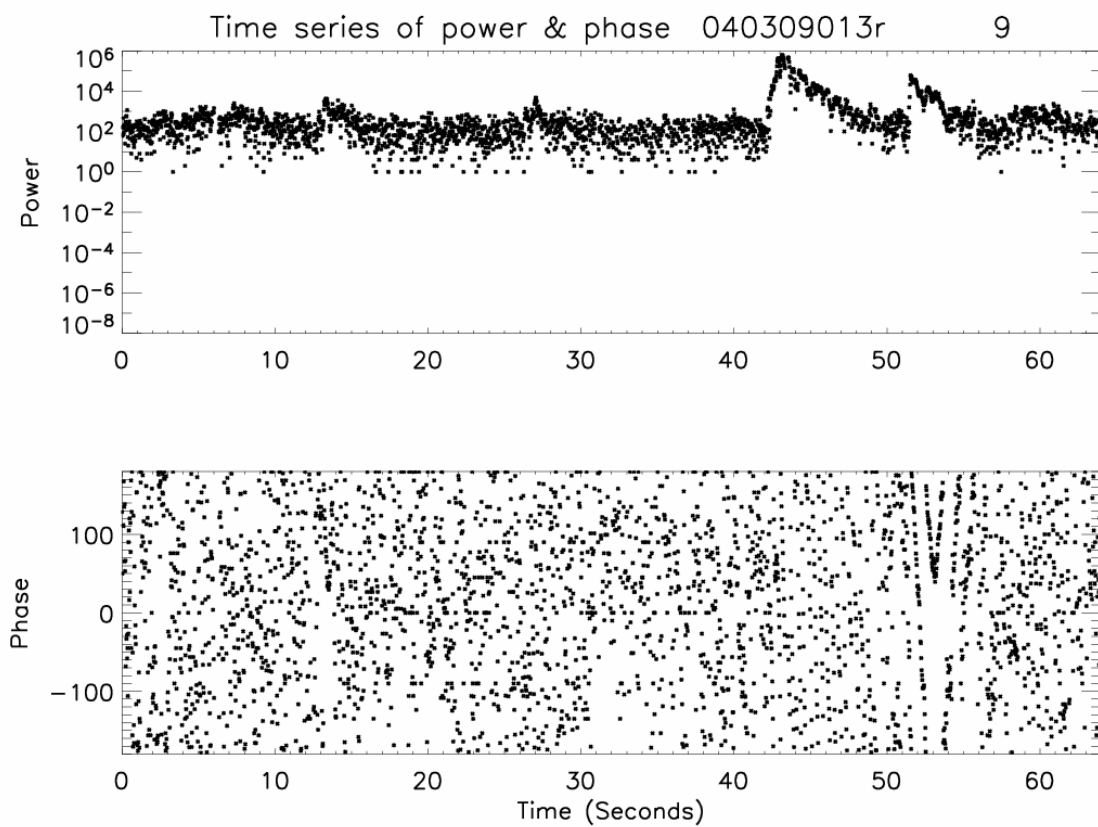

Figure 2.7: Example of meteor echoes detected by TIGER using the TMS operating system

2.2 Radio wave propagation

2.2.1 The effects of the ionosphere

En route to the sea surface and back the radio waves propagate through the ionosphere. Figure 2.8 is a typical daytime profile of electron concentration and neutral temperature versus altitude. The ionosphere can be considered the sum of 4 layers, the D, E, F1 and F2 regions. Table 2.2 gives a summary of all four layers. Each region is characterised by the photochemistry–production and loss processes–that occur there. The peak electron density for each layer forms where diffusive equilibrium is achieved. The photochemistry of the ionosphere is very complicated, and a
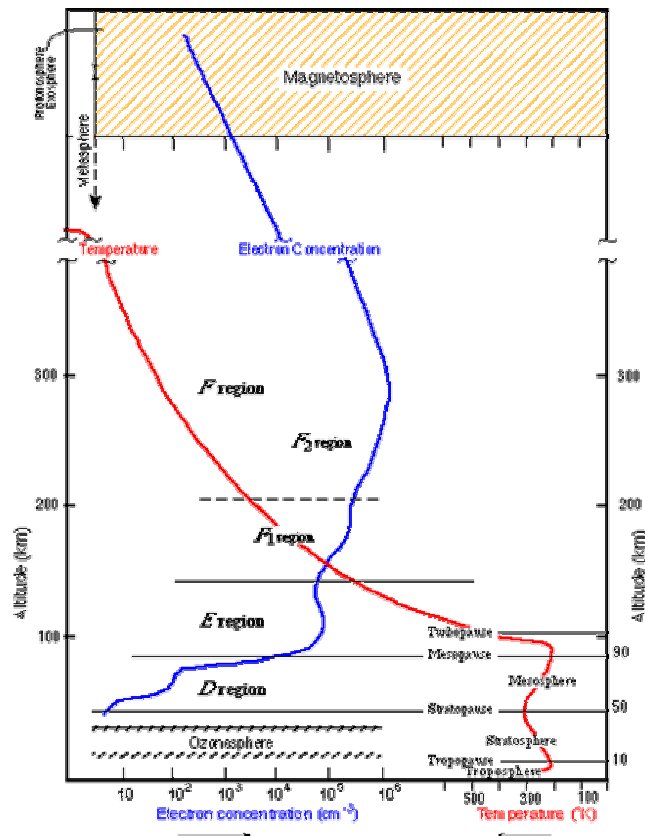
Figure 2.8: Typical daytime profile of electron concentration in the Earth's ionosphere [courtesy of the University of Leicester]

detailed account of them is not needed here. However, the production rate is dependent on the flux of UV and X-rays emanating from the sun. Therefore, the electron concentration profile will vary in accordance with the solar-zenith angle, and will consist of different profiles for day and night. In general, electron densities in the E region peak just after local noon. The electron density is usually lower at night in both the E and F region. However, this is not necessarily so in the F region because transport processes become more important [8].

Table 2.2: Characteristics of the ionosphere [Dr Ian Platt, Physics of the Upper Atmosphere]

Ionospheric region	Altitude	Electron density
D region	60 – 90 km	$10^8 – 10^{10}$ m^{-3}
E region	90 – 160 km	$\sim 10^{11}$ m^{-3}
F1 region	160 – 210 km	$10^{11} – 10^{12}$ m^{-3}
F2 region	250 – 450 km	$\sim 10^{12}$ m^{-3}

Figure 2.9 below shows a schematic diagram of some of the possible propagation modes and regions from which backscatter can occur. The three main types of scatter observed using TIGER and SuperDARN radars in general are half hop, one hop and one-and-a-half hop. Half-hop scatter occurs due to backscatter from irregularities in the ionosphere. One-hop scatter occurs due to that component of the signal which is refracted through the ionosphere without being backscattered by irregularities in the ionosphere. The radio waves are subsequently backscattered from the ground, or the ocean in the case of TIGER. One-and-a-half hop scatter occurs due to the component of the signal that forward scatters from the ocean, and is then subsequently backscattered from ionospheric irregularities.
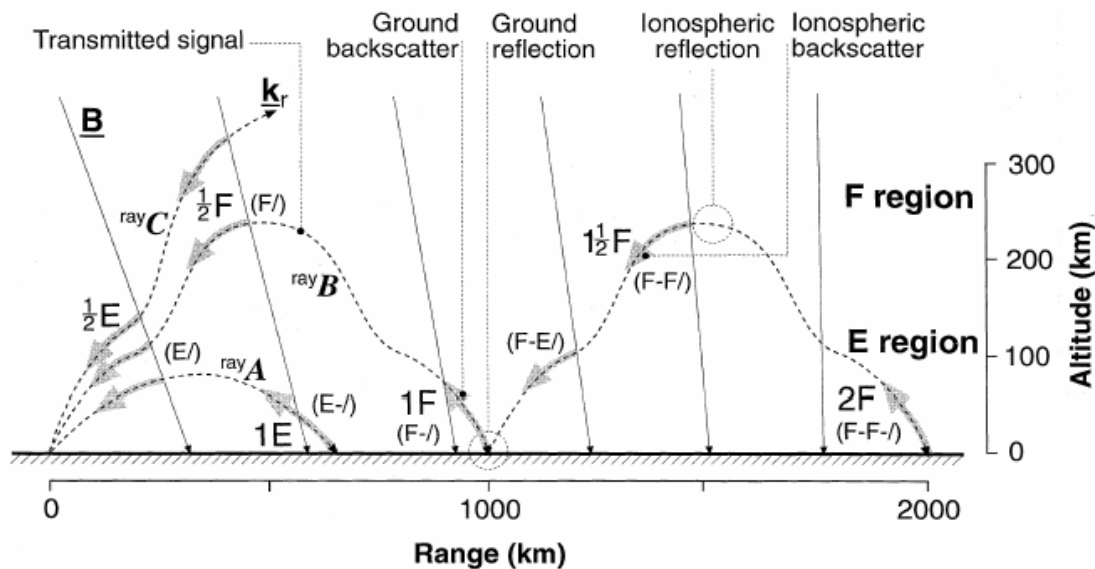
Figure 2.9: A schematic diagram illustrating the basic ionospheric propagation modes and regions from which HF backscatter can occur [15].

If the ionosphere were a perfect mirror at a fixed altitude then there would be no problem determining exactly where the signal came from. This, however, is not the case; the radio waves refract through the ionosphere, and there are often vertical and horizontal gradients in electron density of many scale sizes. This can result in

complicated propagation conditions and modes, including a phenomenon known as "multi-path." This confuses the determination of the true ground range of backscatter, as well as the Doppler characteristics of the echoes.

The complexity of propagation for even relatively simple conditions can be seen in Figure 2.10. The group path is the time taken for the backscattered signal to return divided by two and multiplied by the speed of light. A group path is associated with every propagation mode and ray. Sometimes, two pulses with the same group path will emanate from completely different areas. The absence of pure propagation channels can have the detrimental effect of de-cohering echo phases.

There are, however, means of discerning where an echo comes from. For example, the FITACF algorithm takes into account the Doppler velocity and spectral width to decide whether an echo emanates from the ionosphere or "ground." Basically, if the Doppler velocity and spectral widths are less than 30 m s^{-1}, the echo is flagged as ground scatter. However, especially in the case of a subauroral radar like TIGER, many ionospheric echoes are probably flagged as ground scatter. As will become apparent, the results of this thesis represent an important contribution to the unambiguous identification of ionospheric and ground scatter.

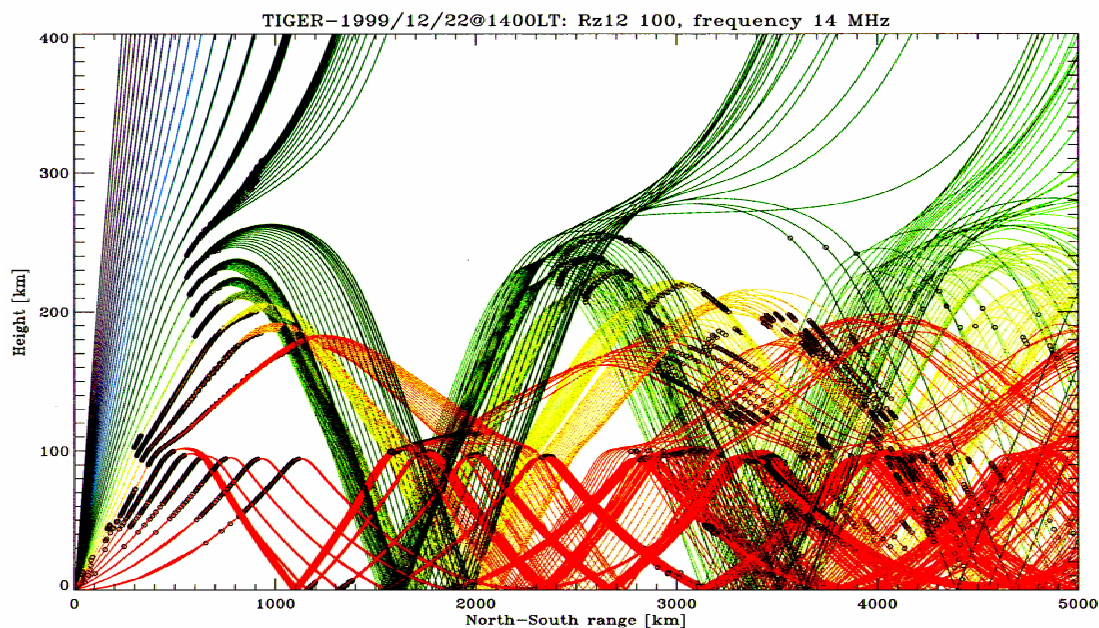Figure 2.10: Superimposed true trajectories for take-off and true azimuth angles from 0° to 60° in 2° steps and from 130° and 250° in 5° steps, respectively. The rays were colour-coded according to take off angle. The black circles locate possible backscatter centres. The simulation was performed for a sunspot number of 100 and a frequency of 14 MHz at 14:00 LT on the 22nd of December 1999 [16].

To further complicate the matter, the ionosphere in general is non-static, imparting a Doppler shift on the radio waves as they travel through the ionosphere. Horizontal motions of the ionosphere will affect the propagation. However, the motion is usually considered to be constant over the short time it takes to transmit and receive an echo (in the order of milliseconds). Hence the radio waves will be red shifted one way and blue shifted the other, giving a net zero Doppler shift for one hop backscatter [17] [18]. However, the vertical motion of the ionosphere will impart a net blue shift when moving down, and a net red shift when moving up. The main causes of vertical motion in the ionosphere include acoustic gravity waves, ULF waves, and the transport of ionospheric irregularities. To what extent this affects the frequency is given by [19]:

$$\Delta v = \frac{\lambda_{radar}}{2} \Delta f$$

(2.1)

The Bragg spectrum of sea echoes will be Doppler shifted by the net vertical ionospheric motions occurring during an integration time. These Doppler shifts will be broadened by both the spread of vertical ionospheric motions and the presence of multi-path during the integration time. However, accurate surface current measurements can still be obtained by averaging away the ionospheric Doppler shifts, or subtracting them by using ground echoes to calibrate the zero-Hz Doppler shift.

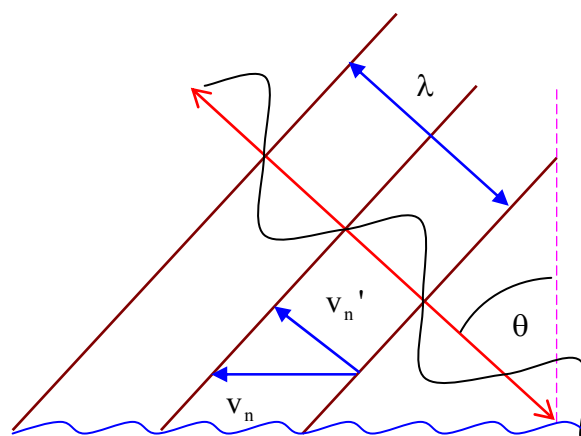### 2.2.2   Derivation of the Bragg frequency for sky-wave propagation

Figure 2.11: Geometry illustrating the backscatter of oblique sky waves from sea waves

Although equation (2.1) is accurate for surface-wave measurements, it does not describe measurements made at any angle of incidence. For this reason, the geometry of the situation is considered in Figure 2.11.

In can be seen that the apparent phase velocity and the phase velocity of the sea waves are related by:

$$v_n' = v_n \sin(\theta) \tag{2.2}$$

where v_n is the true phase velocity, v_n' is the measured phase velocity, and θ is the angle of incidence. Substituting equation (2.2) into equation (2.1) gives:

$$f_n = \frac{2 v_n \sin(\theta)}{\lambda} \tag{2.3}$$

The phase velocity v_n is given by the gravity wave dispersion relation for surface waves in deep water [12]:

$$v_n = \sqrt{\frac{g L_n}{2\pi}} \tag{2.4}$$

where g is the acceleration due to gravity, and L_n is the wavelength of the ocean waves satisfying the Bragg condition:

$$L_n = \frac{n\lambda}{2 \sin(\theta)} \tag{2.5}$$

where, n is an integer greater then zero, λ is the wavelength of the radio wave, and again, θ is the angle of incidence. Substituting (2.5) into (2.4) gives:

$$v_n = \sqrt{\frac{n g \lambda}{4\pi \sin(\theta)}} \tag{2.6}$$

Substituting (6) into (3) gives:

$$f_n = \pm\sqrt{\frac{n g \sin(\theta)}{\pi \lambda}} \tag{2.7}$$

Which can be further related to the frequency transmitted by the radar by the relation:

$$f_n = \pm\sqrt{\frac{n g f \sin(\theta)}{\pi c}} \tag{2.8}$$

This equation gives the first-order Bragg frequency for oblique incidence. Generally, only the first (n=1) first-order need be taken into account, as the power greatly diminishes for n>1. An account of the theory of second-order electromagnetic and hydrodynamic scattering from the sea surface is beyond the scope of this thesis.

2.2.3   Variation of the Bragg frequency with group path

The Bragg equation [11] shows that the angle of incidence, θ, is important in determining the wavelength of the observed ocean waves:

$$2L_n \sin(\theta) = n\lambda \tag{2.9}$$

where L_n is the wavelength of the ocean waves, λ is the wavelength of the radio waves, and n is a positive integer. There are a number of ways of determining how this angle varies with group path, the most simple of which is to consider the ionosphere as a flat mirror-like surface that reflects radio waves with equal angles of incidence and reflection. The simplest flat Earth geometry is shown in Figure 2.12.
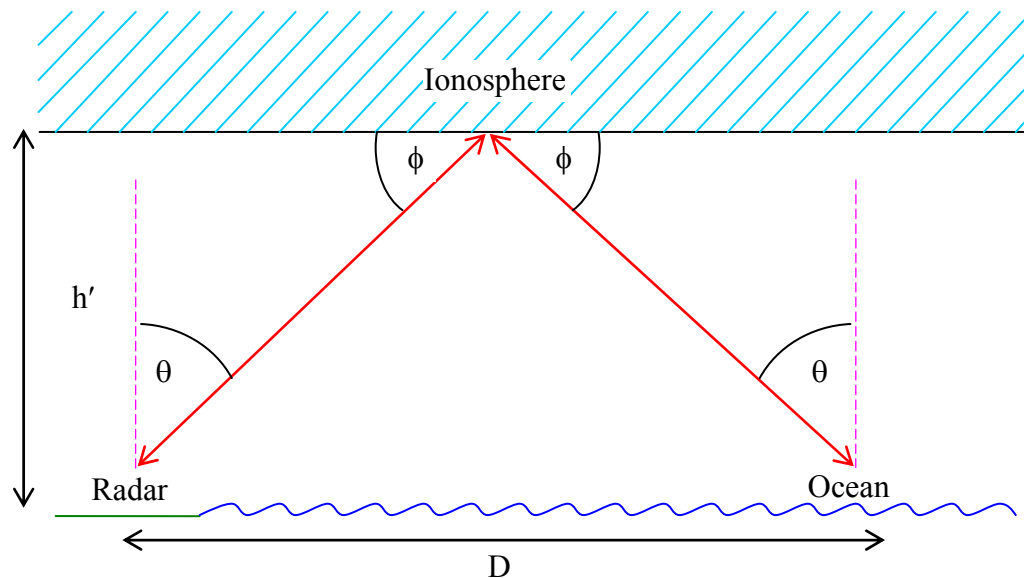

Figure 2.12: A mirror like reflection off a flat ionosphere

A radio wave emitted from the radar is reflected off the ionosphere through an angle ϕ and then is incident on the sea surface at angle θ. The angle θ is simply given by:

$$\theta = \arctan\left(\frac{D}{2h'}\right) \tag{2.10}$$

where D is the true ground range, in the order of 1000 to 2000 km for this experiment. h′ is the virtual height of the ionosphere, varying from approximately 150 km for the E layer to approximately 400 km for the F2 layer. The phenomenon that is best approximated to a mirror like surface is sporadic E which often consists of a thin layer of high electron density caused by electric fields or wind shears forcing the plasma together [12]. However, sporadic E is a transient phenomenon, and usually the peak electron density occurs in the F2 layer. Assuming a virtual reflection height of 400 km

and the backscattered signal has a ground range of 1500 km, the angle of incidence is 61.9°. However, the height of the peak electron density often changes; an increase in the peak height of 50 km will cause the angle of incidence to decrease by 2.9° at the same ground range. Likewise, the angle of incidence will decrease by 6.27° as the ground range changes from 2000 km to 1500 km.

A reasonably accurate estimation of the angle of incidence is obtained by considering a mirror approximation with variable virtual height, h′, whilst taking into account the curvature of the Earth. Validity of the mirror approximation follows from Breit and Tuve's theorem [13]. Figure 2.13 shows the curved Earth geometry relating the radius of the Earth, the virtual reflection height and the group path to the elevation angle.
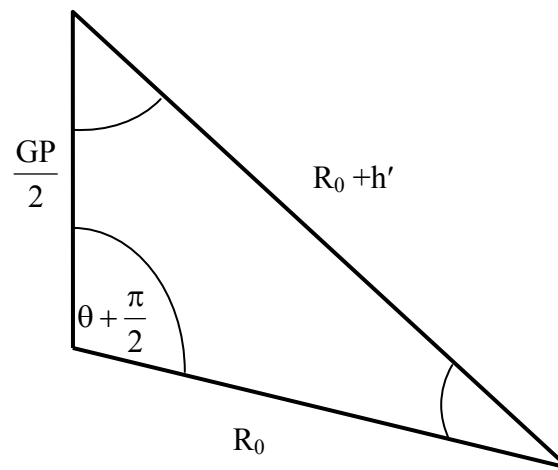
Figure 2.13: Geometry relating the radius of the earth, R_0, reflection height, h′, and group path, GP, to elevation angle, θ.

Using the cosine rule we obtain the expression:

$$\left(R_0 + h'\right)^2 = R_0{}^2 + \left(\frac{GP}{2}\right)^2 - R_0 GP \cos\left(\theta + \frac{\pi}{2}\right)$$ (2.11)

where R_0 is the radius of the Earth. Solving equation (2.11) for θ gives:

$$\theta = \arcsin\left(\frac{8R_0 h' + 4h'^2 - GP^2}{4R_0 GP}\right)$$ (2.12)

The angle of incidence, θ′, is related to the elevation angle, θ, by:

$$\theta' = \frac{\pi}{2} - \theta$$ (2.13)

Substituting equation (2.12) into equation (2.13) gives the angle of incidence in term of group path and virtual height:

$$\theta' = \frac{\pi}{2} - \arcsin\left(\frac{8R_0 h' + 4h'^2 - GP^2}{4R_0 GP}\right) \qquad (2.14)$$

Equation (2.14) has been evaluated for various group paths and virtual heights in Table 2.3. First order Bragg frequencies have been calculated using equation (2.8).

Table 2.3: Angle of incidence and Bragg frequencies shown for various group paths and virtual heights.

Group path	θ_1 (h' = 150 km)	f_{b1}	θ_2 (h' = 400 km)	f_{b2}
315 km	17.97°	0.197 Hz	–	–
495 km	53.57°	0.317 Hz	–	–
675 km	64.96°	0.337 Hz	–	–
855 km	71.25°	0.344 Hz	21.33°	0.213 Hz
1035 km	75.35°	0.348 Hz	40.83°	0.286 Hz
1215 km	78.33°	0.350 Hz	50.84°	0.312 Hz
1395 km	80.62°	0.352 Hz	57.54°	0.325 Hz
1575 km	82.47°	0.352 Hz	62.48°	0.333 Hz
1755 km	84.02°	0.353 Hz	66.34°	0.339 Hz
1935 km	85.35°	0.353 Hz	69.48°	0.343 Hz
2115 km	86.53°	0.354 Hz	72.11°	0.345 Hz
2295 km	87.58°	0.354 Hz	74.36°	0.347 Hz
2475 km	88.53°	0.354 Hz	76.33°	0.349 Hz
2655 km	89.41°	0.354 Hz	78.07°	0.350 Hz
2835 km	>90°	–	79.64°	0.351 Hz
3015 km	>90°	–	81.06°	0.352 Hz
3195 km	>90°	–	82.36°	0.352 Hz
3375 km	>90°	–	83.56°	0.353 Hz

There can be no ground scatter for a signal propagating to a virtual height of 400 km that has a group path less then 800 km; this is consistent with Table 2.3. Also, for a virtual height of 150 km, group paths of more then 2655 km are not possible as they

will be unable to see "over-the-horizon". For the majority of group paths the predicted Bragg peaks are very similar; that is, they are within 0.05 Hz of the surface-wave limit. Therefore, the majority of first-order backscatter from the sea will be close to the predicted limits for $\theta = 90°$.

Figure 2.14 is a contour plot of elevation angle versus group path and time. These results were obtained by fellow honours student, Mr. Shane Martin, using ray tracing techniques through the International Reference Ionosphere (IRI). The effects of Traveling Ionospheric Disturbances (TIDs) have been included in these results. Figure 2.14 is particularly relevant as the results are for TIGER beam 4 on the 9th March 2004. The majority of data analysed in this thesis was recorded in early March. The diurnal variation of elevation angles and group paths are basically consistent with our observations.
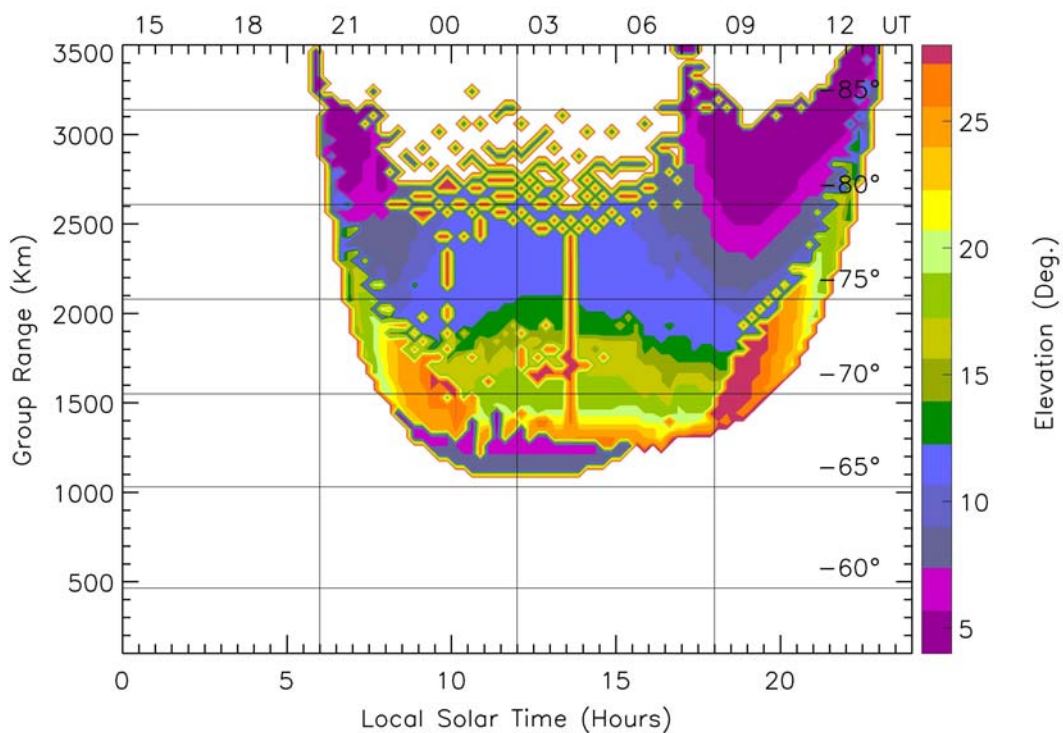

Figure 2.14: Contour plot of elevation angle versus group path and time. These ray tracing results are for TIGER beam 4 and the IRI model for the 9th March 2004 [courtesy of Mr. Shane Martin].

3 Experiments and Data Analysis

3.1 Discretionary mode campaigns

3.1.1 Installation of the new TMS software

A new radar operating system known as the "TMS" version of the normal Super-DARN radar operating system, RST/ROS V1.03 [23], was installed and tested on TIGER. The TMS operating system still supports all the previous modes of operation which utilise the FITACF algorithm [14], whilst concurrently extracting high time resolution time series of the amplitudes and phases of echoes received using the standard SuperDARN seven-pulse pulse sets normally used to construct ACFs. Access to long, complex time series were required to achieve the Doppler resolution necessary to resolve the Bragg peaks that characterise sea wave backscatter. Depending on the purity and stability of the HF sky-wave channel, time series of length 32 s, 64 s, 128 s and perhaps more, are desirable.

The installation and testing of the new software was a multi-part process. First, the operating system was installed on the dummy TIGER radar which replicates the operation of the real radar, except the transmitters are terminated by dummy 50 Ω loads [Dr Harvey Ye, private communication]. This was done to minimise the chances of the TMS operating system causing problems with the real radar. Next, once the TMS operating system was working satisfactorily on the dummy radar, including full hardware emulation, it was installed and tested on the real radar during discretionary time. This was to ensure that any problems that may arise could be solved before common mode operations resumed.

As it turned out, the primary attempt to run a TMS radar control program crashed the real radar. This was due to an overflow error in the main program. A 128-s integration time was attempted and was later found to be greatly in excess of the ~22-s limit currently built into the operating system [Dr Sessai Yukimatu, private communication]. Once the problem was realised, the TIGER radar was re-booted, the

three discretionary mode campaigns were successfully tested, and then finally executed.

Without the in-depth understanding of how the new TMS operating system would perform, it was decided that a variety of campaigns would be run. In this regard, a range of operating parameters were tested so as to best enable the deduction of solutions to any problems that might arise.

3.1.2   Discretionary mode campaign A

The first discretionary mode campaign was run using the radar control program "fast_scan_tms" between 23:30 UT, 8th March 2004 to 09:50 UT, 10th March 2004. The chosen operating parameters for the first of the discretionary mode campaign were selected with prudence; that is to say, they were similar to those used during common mode operation. The parameters were chosen in such a way as to minimise the possibility of the new software failing. In this regard, the integration time was set to 6 s, a standard choice for common mode operations. Soundings were only performed on one beam so that continuous, long time series could be obtained by concatenating the results obtained using successive 6 s integration times.

As previously mentioned, the initial release of the TMS operating system limited the integration time to ~22 s and access to a reliable radar control program with the capability to perform multiple integrations before advancing to the next beam was not available. Thus measurements were not made on all 16 beams. For this pilot study, beam 4 was chosen for data collection because it was aligned directly towards the magnetic pole, and had been used for previous ray tracing studies that could help us understand the propagation conditions for the sea scatter [24].

Importantly, the frequency band was set to 12.05 to 12.10 MHz for all three campaigns. 12 MHz has proven to be a good all round working frequency for numerous studies. However, ideally the operating frequency should be determined in real time to optimise the purity and stability of the sky-wave channel, as well as the strength and coverage of sea scatter. The frequency was constrained to within a 50 kHz band to help ensure that time series elements remained coherent from one

integration time to the next. A frequency of 12.0 MHz Bragg scatters from first-order sea waves of length 12.45 m, a modest scale size for waves in the Southern Ocean.

Lastly, the interferometer used to estimate elevation angle was turned off to halve the amount of data collected. During testing, the TMS operating system produced several giga-bytes of data per day, and this stretched the existing data storage and transmission capacity beyond its limit.

3.1.3   Discretionary mode campaign B

The second discretionary mode campaign was run using the radar control program "fast_scan_tms" between 02:40 UT, 19th March 2004 to 06:00 UT, 20th March 2004. This discretionary mode campaign was similar to the first, except with two main differences. First, the single beam chosen was beam 7 which most closely points towards geodetic south. This seems a more reasonable choice for oceanographic studies which are normally posed in the geodetic reference frame. Next, the integration time was reduced to 2 s to test whether more regular time series data could be obtained using very short integration times.

3.1.4   Discretionary mode campaign C

The third discretionary mode campaign was run using the radar control program "fast_scan_tms" between 16:00 UT, 20th March 2004 to 06:30 UT, 21st March and between 02:30 UT, 22nd March 2004 to 05:50 UT, 22nd March 2004. Again, beam 7 was used, but this time the integration time was changed to 16-s. The reasoning behind this was to obtain times series data of the maximum possible length permitted by the TMS operating system, whilst still being a power of 2, and thus suitable for subsequent Fourier analysis. Likewise, the effect of using 2 s, 6 s and 16 s integration times upon Doppler resolution could be examined. As will be seen, the TMS operating system generated coherent time series elements, which were coherent from one integration time to the next, so the actual choice of integration time was not critical, nor was it necessary to work with powers of two.

3.1.5   Summary of the discretionary mode campaigns

Three discretionary mode campaigns were undertaken, each with the same goal, namely to show that TIGER can achieve the Doppler resolution necessary to resolve the Bragg peaks which characterise ocean backscatter. For all three campaigns, the same operating frequency was used. The same standard 45-km transmitter pulse width and range gates were also used, namely the first range for data collection was set to180 km and thereafter 70 range gates separated by 45 km. Table 3.1 summarises the main changes in radar operating parameters.

Table 3.1: A summary of the discretionary mode campaigns

Discretionary mode campaign	Integration time (seconds)	Beam number	Frequency (MHz)
A	6	4	12.05 - 12.10
B	2	7	12.05 - 12.10
C	16	7	12.05 - 12.10

3.2   Data Analysis

3.2.1   Observation of Bragg type Doppler spectra

As was stated earlier, the aim of this project was to observe the backscattered signal from sea waves using the TIGER SuperDARN radar, in such a way as to deduce relevant sea state properties of the Southern Ocean. It is important to locate preferential regions of backscatter from the sea surface. Figure 3.1 shows a summary plot of the data collected during the first of the discretionary mode campaigns commencing on the 8th of March 2004. A summary plot is a means of quickly and concisely colour coding the data collected in terms of backscattered power (signal-to-noise ratio), line-of-sight Doppler velocity and spectral width. Figure 3.1a is colour coded to represent the power of the backscattered signal in decibels. Figure 3.1b is colour coded to represent the line-of-sight velocities in meters per second, and Figure 3.1c is colour coded to represent the spectral widths in meters per second. Summary plots of all three campaigns are collated in Appendix A.
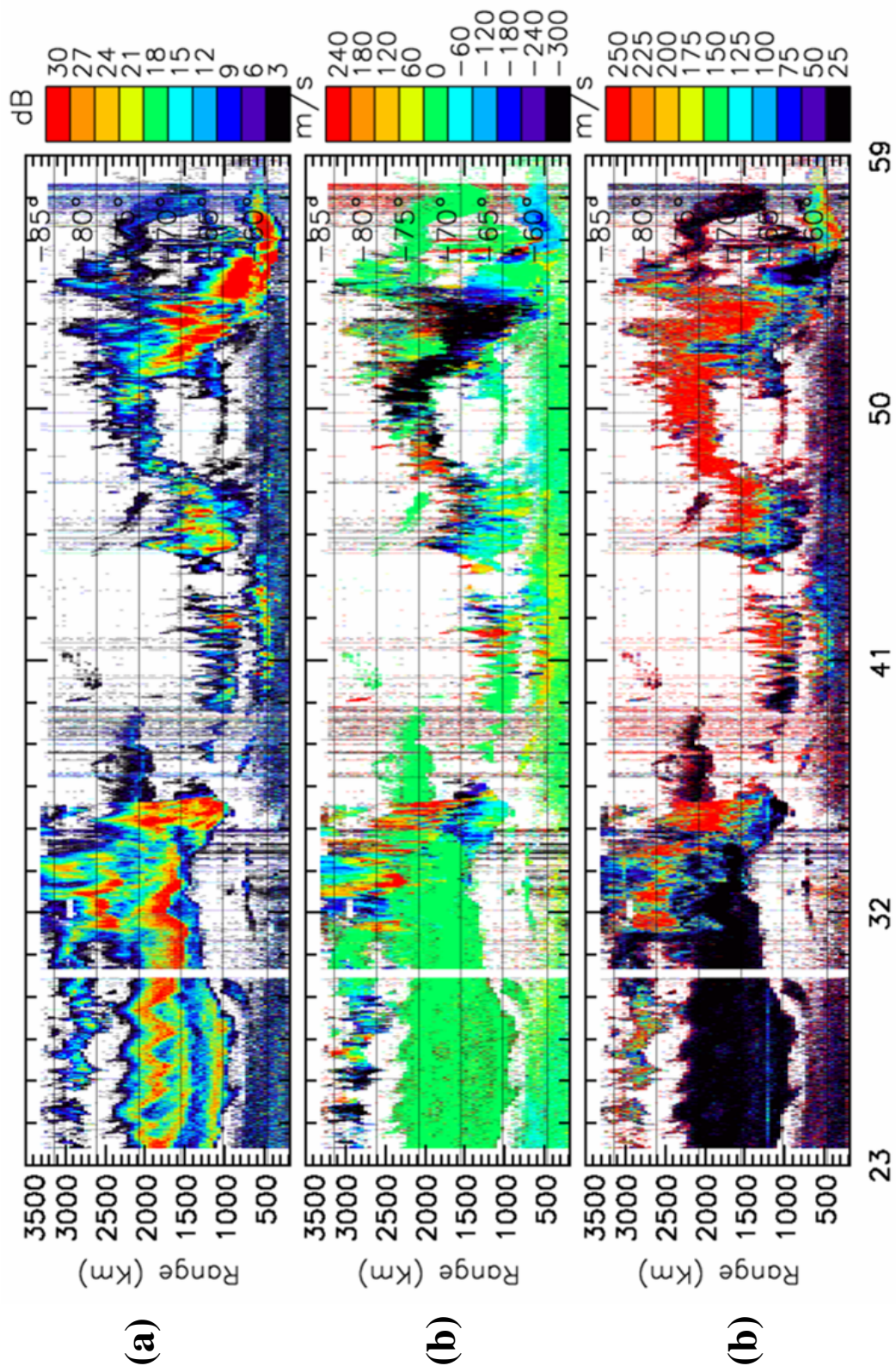
Figure 3.1: Summary plot of discretionary mode campaign A showing the backscattered power (a), line-of-sight Doppler velocities (b) and spectral widths (c).

Regions of signal backscattered from the sea surface can be quickly inferred from Figure 3.1 by noting areas that have a low line-of-sight Doppler velocity, indicated by green in Figure 3.1b and a corresponding low spectral width, indicted by black in Figure 3.1c. The region where this condition is satisfied to the greatest extent corresponds to ~23–34 UT, or the mostly sunlight hours of ~09 am to 08 pm local time, and over ranges of ~900–2400 km in group path. This region is characterised by three distinct bands of high backscattered power, in all likelihood attributed to different propagation conditions. There is clear evidence of an atmospheric gravity wave during this period at ranges of 1700–2000 km
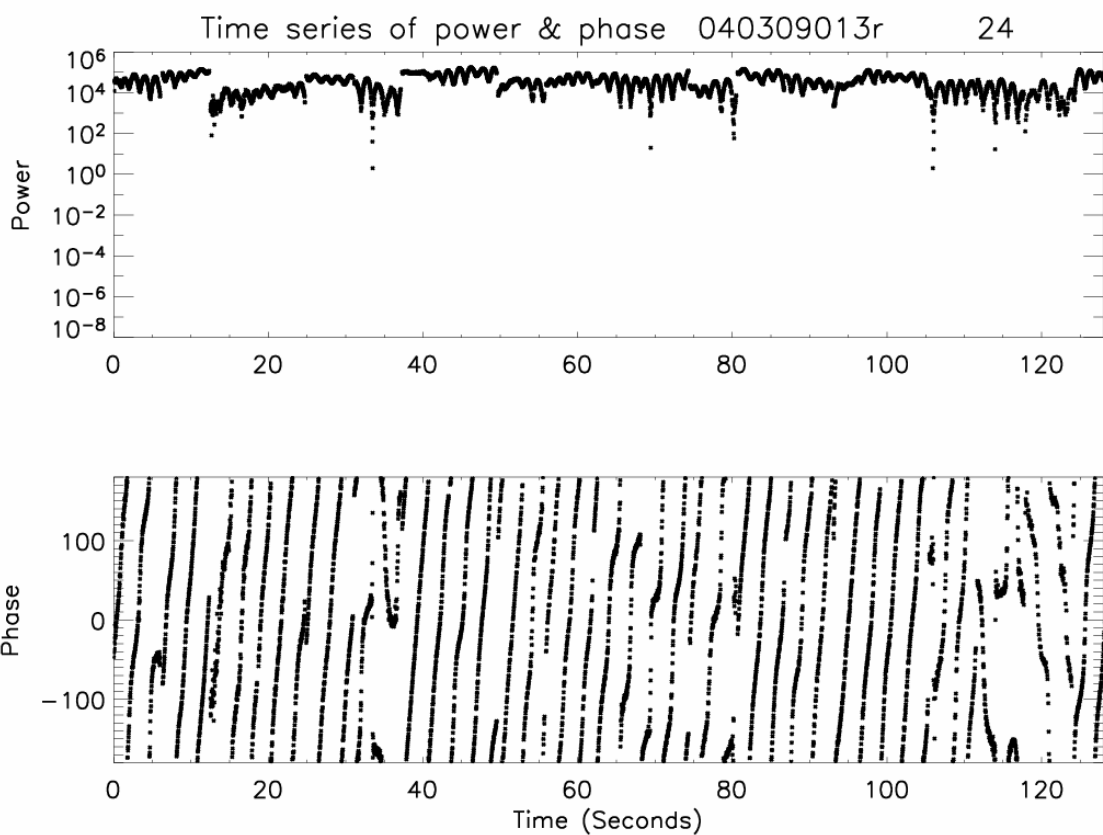

Figure 3.2: Time series of power and phase starting at 01:30 UT on the 9th of March 2004, for range bin 24 which has a corresponding group path of 1080 km.

With a clear picture of where the regions dominated by sea scatter reside, a "raw" time series analysis of specific regions was undertaken. By "raw" time series, we mean data that contains the in-phase and quadrature values returned by each pulse of the radar, before any ACFs have been calculated. The quantity of data generated by the TMS operating system was vast, so it could only be surveyed for interesting results. Two one-hour intervals were considered for each discretionary mode campaign and a time series of power and phase was plotted at each range bin and for

128 seconds commencing at each 10 minute interval within each one hour interval. Figure 3.2 shows one such plot for discretionary mode campaign A; it shows the results for range bin 24 and for 128 seconds starting at 01:30 UT on the 9th March 2004. Figure 3.2 is a clear example of the time series of power and phase expected for a signal backscattered from the sea. The power is relatively constant although with some periodicity; the fluctuations in power can be attributed to the change in gain of the radar at the integration time boundaries. There is also a uniform phase periodicity of approximately 3 seconds, as expected for Bragg-type scattering.
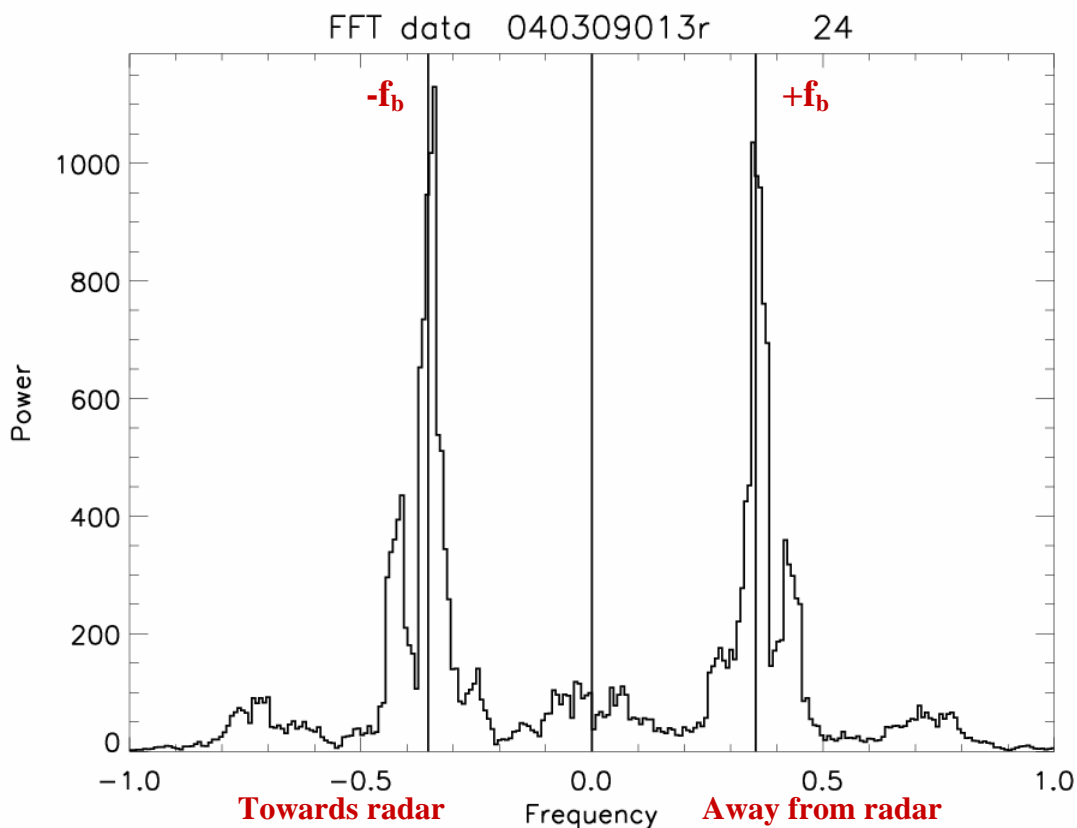

Figure 3.3: Doppler spectrum produced by taking the FFT of the time series of in-phase and quadrature components corresponding to the results shown in Figure 3.2. The vertical lines represent the predicted Bragg frequencies for direct propagation.

The ocean backscatter can be further characterised by taking the Fast Fourier Transform (FFT) of the time series of in-phase and quadrature amplitudes (i.e., the time series of power and phase shown in Figure 3.2) to produce a Doppler spectrum as seen in Figure 3.3. The raw time series analysis technique produces in-phase and quadrature amplitudes separated by uneven time intervals. To perform an FFT there needs to be an even time series and this was obtained by averaging in-phase and quadrature amplitudes over 0.25 s intervals. This provides the even time series necessary without compromising resolution of Bragg peaks, as this provides a Nyquist

frequency of ± 2 Hz. In Figure 3.3, the vertical lines represent the predicted Bragg frequencies for surface-wave propagation. The Bragg frequencies should be slightly less for sky-wave propagation and oblique incidence on the sea surface. Clearly, the observations are consistent with prediction. Resolution of the main Bragg peaks means that we are able to deduce certain sea state properties, namely the prevailing wind and wave direction, and the line-of-sight velocity of surface currents.

Although not as pronounced, there are clear second-order side lobes that can be used to derive other properties of sea state, namely wave heights and the scalar wave spectrum. These results would not be attainable by taking the FFT of the ACFs to construct the Doppler spectra, because only a single poorly resolved peak would be observed. Figure 3.3 is clear testimony to the fact that the raw time series approach provides an excellent method for analysing sea scatter.
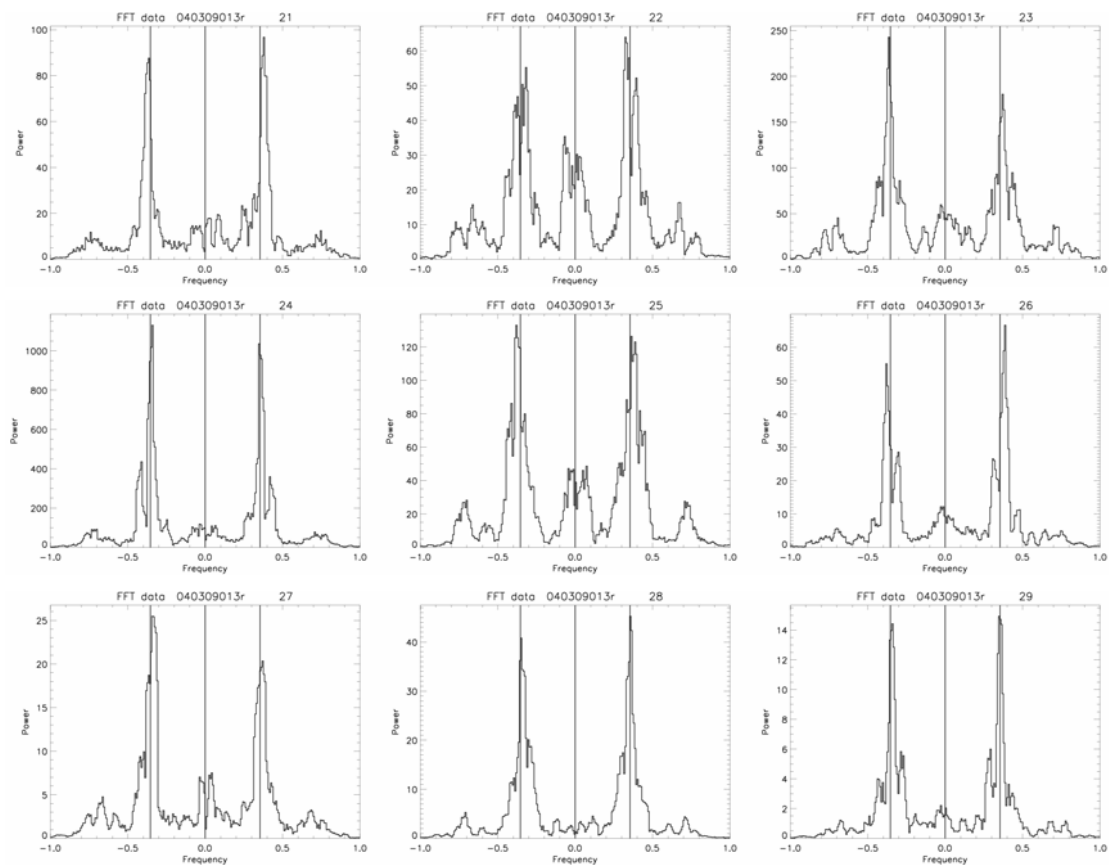

Figure 3.4: Doppler spectra plots for range bins 21 to 29 (900 to 1305 km) obtained using time series of length 128 s starting at 01:30 UT on the 9 March 2004.

The result in Figure 3.3 is reproducible over multiple ranges for a given time, as can be seen in Figure 3.4 which shows nine Doppler spectra plots for ranges from 900 km to 1350 km. They all use time series of length 128 s starting at 01:30 UT on the 9th March 2004.

It can be clearly seen that there are two distinct Bragg peaks occurring near to the predicted Doppler frequencies over all ranges. The ratio of the Bragg peaks is clearly not a constant for all ranges. This could be due to differences in the state of the ocean at these ranges, however, propagation conditions cannot be ruled out as a source of this ambiguity. In some cases a zero Hz peak can be observed. In all likelihood this is ground scatter detected from a back lobe. The plot for range bin 27 (bottom left) shows evidence for possible surface currents, however, ULF gravity waves in the ionosphere cannot be ruled out as a cause of the net Doppler shift. Some cases show Bragg peaks outside the expected limits; the forerunning explanation for this is that the phase did not maintain strict coherency over small gaps from one integration time to the next.

Further evidence, for the reproducibility of these results for all discretionary campaigns, is compiled in Appendix B.

3.2.2 Calculation of wind and wave directions and surface currents

A major outcome of this analysis is the capability to calculate the prevailing wind and wave direction and line-of-sight velocity of surface currents using the first order peaks in the Doppler spectra. To achieve statistical significance, numerous Doppler spectra of 128-s intervals throughout ~30 min must be averaged. However, the process through which wind and wave directions and surface currents are calculated is independent of the time interval considered.

When determining the prevailing wind direction, it can be assumed that for relatively short waves such as those being observed using a frequency of 12.05 MHz; the prevailing wind direction is closely aligned to the dominant wave direction. The directional sea spectrum can be modelled using an equation of the form:

$$G(f,\theta) = \alpha + (1-\alpha)\cos^{s(f)}\left[\frac{(\theta - \theta_{dsd})}{2}\right]; \quad -\pi \leq \theta < \pi \tag{3.1}$$

where θ_{dsd} is the dominate sea direction, α is included to account for a small amount of upwind–propagating energy and $s(f)$ is known as the spread parameter [25]. Assuming α, $s(f)$ and θ_{dsd} are independent of frequency, a simplified version of directional sea spectrum equation can be seen below for $\alpha=0.01$ and $s(f)=2$.

$$G(f,\theta) = 0.01 + 0.99\cos^2\left(\frac{\theta}{2} - \frac{\pi}{4}\right); \quad -\pi \leq \theta < \pi \tag{3.2}$$

The relative heights of the Bragg peaks are controlled by the directional sea spectrum and can be denoted by A and B, as in Figure 3.5. Figure 3.6 is a graphical representation of equation (3.2), with a prevailing wind and wave direction towards the top of the page. The solid black lines represent the amplitudes of the observed Bragg peaks for a prevailing wind direction at some angle ($\pi/2-\theta$) to the radar.
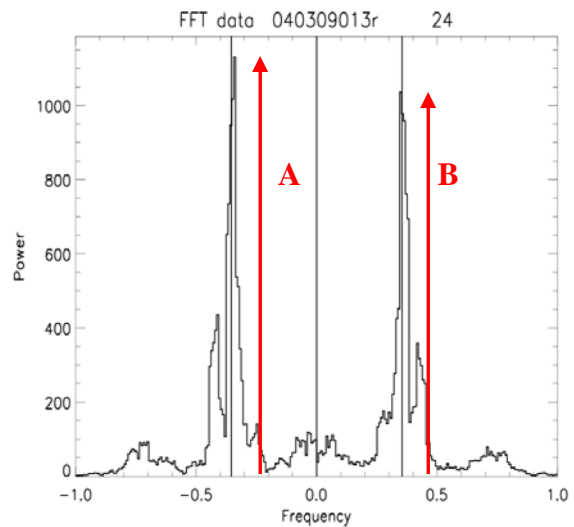

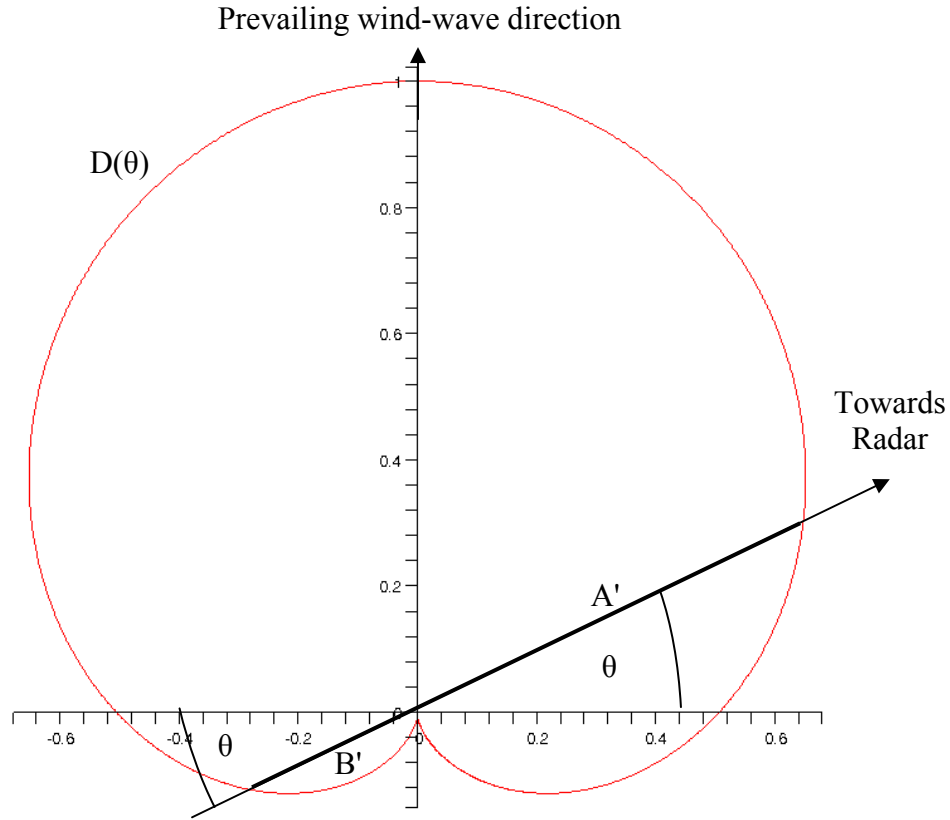Figure 3.5: A and B are the heights of the approaching and receding Bragg peaks, respectively.

Figure 3.6: Directional sea spectrum model using equation (3.2) with a prevailing wind and wave direction towards the top of the page. The solid black lines, A′ and B′ represent the amplitudes at $-f_b$ and $+f_b$, respectively.

A and B, the powers of the approaching and receding Bragg peaks, respectively, are related to the A′ and B′, the amplitudes of the directional sea spectrum for a given angle by:

$$\frac{A}{B} = \sqrt{\frac{A'}{B'}}$$

(3.3)

The following relationship for θ must be solved to determine the angle at which the wind is propagating relative to the radar:

$$\frac{A'}{B'} = \frac{D(\theta)}{D(\theta + \pi)}$$

(3.4)

For example, for θ=0,180°, the prevailing wind direction is perpendicular to the radar beam direction and A=B. For θ=90°, the prevailing wind direction is towards the radar and A>>B. For θ=–90°, the prevailing wind direction is away from the radar and A<<B.

As a sample calculation, the ratio of Bragg peaks in Figure 3.5 is given by:

$$\frac{A}{B} = \frac{1125}{1037} \qquad (3.5)$$

Relating equation (3.5) to equations (3.3) and (3.4) gives:

$$\frac{D(\theta)}{D(\theta + \pi)} = \sqrt{\frac{1125}{1037}} \approx 1.04157 \qquad (3.6)$$

Solving equation (3.6) gives: $\theta = 0.02077$ or $0.02077 \pm \pi$ radians or $\theta = 86.88 \pm 90°$. This means the prevailing wind direction in this case was close to perpendicular across the radar beam. The directional ambiguity can be resolved with the addition of TIGER Unwin and is discussed in Chapter 4.21.

Prevailing wind and wave directions can be easily calculated from the ratio of Bragg peaks using a raw time series and Doppler spectrum analysis technique, so long as a reasonable model for the directional sea spectrum is used. It is possible to calculate statistically significant wind and wave directions for all 16 beams and over multiple ranges with half hourly resolution; this will be further discussed in Chapter 4.2.1.

Line-of-sight surface currents can be determined simply from the offset in the Bragg peaks; that is, where both approaching and receding Bragg peaks are shifted, either positively or negatively on the frequency axis. This change in frequency, Δf, can be related to the radial component of the surface current, Δv, by: [1]

$$\Delta v = \frac{\lambda_{radar}}{2} \Delta f \qquad (3.7)$$

In general, however, there is no means of distinguishing a Doppler shift due to a radial surface current from that of ionospheric motion over a short integration time. Other workers have used ground echoes from islands to identify and remove the Doppler shift due to ionospheric motion. As there were no islands in TIGER's field of view during this study, we adopted the following approach for illustrative purposes only. The occurrence of ground echoes in back lobes were observed in many Doppler spectra, so we assumed that the ionospheric Doppler shift was the same for signals detected via the main and back lobes. Of course, this is not an accurate assumption, but it does allow us to illustrate how radial surface currents could be calculated if islands had been in the radar field of view.

Figures 3.7a and 3.7b show typical Doppler spectra for (a) Bragg peaks that have been mostly shifted by a radial surface current towards the radar and (b) Bragg peaks that have been shifted by larger ionospheric motion. Figure 3.7b is considered to have been red shifted partly due to the ionosphere, because the zero Hz or ground peak has also been red shifted. This is consistent with a net rising ionosphere over the period of integration.

Neglecting any ionospheric contribution for the case in Figure 3.7a, the change in frequency is simply given by:

$$\frac{A + B}{2} = \Delta f \tag{3.8}$$

where, A is the frequency as which the negative Bragg peak occurs, B is the frequency at which the positive Bragg peak occurs, and Δf is the change in frequency.
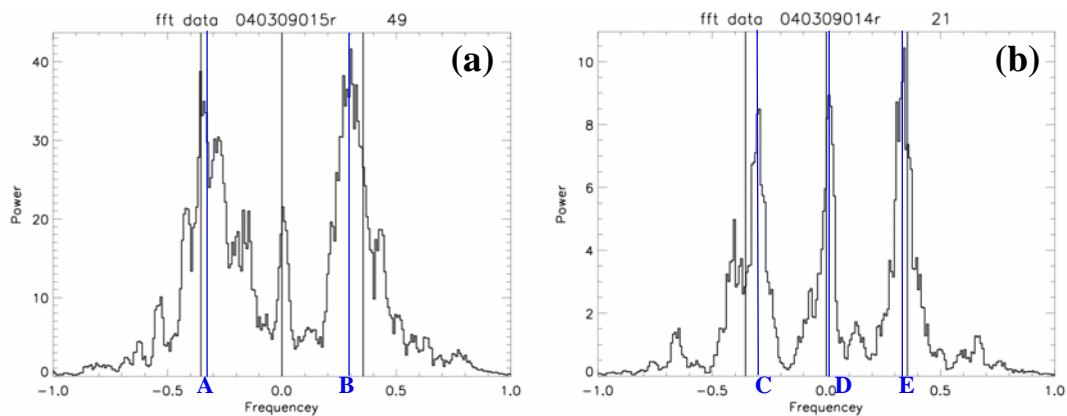

Figure 3.7: Shows Doppler spectra where (a) there is a radial surface current towards the radar, and (b) there is an unusually strong red shift of the spectral peaks, most likely caused by a rising ionosphere.

Equation (3.8) relates to the radial component of the surface current via the relation:

$$\Delta v = \frac{\lambda_{radar}(A + B)}{4} \tag{3.9}$$

As an example the vales of A and B in Figure 3.7 are –0.330 Hz and 0.306 Hz, respectively, with λ_{radar} in this case being 24.9 meters. This gives a radial surface current towards the radar of 14.94 cm s^{-1}.

In the case of the example where a strong ionospheric red shift is also present (Figure 3.7b), its effect needs to be taken into account when solving for the radial velocity of the surface currents. This is done by assuming that both Bragg peaks are offset from

their surface current position by an ionospheric red shift equivalent to the red shift of the ground peak. This can be expressed by the following relationship:

$$\Delta v = \frac{\lambda_{radar}\left(\left(C - D\right) + \left(E - D\right)\right)}{4} \qquad (3.10)$$

In the case of Figure 3.7b, C, D and E were–0.294 Hz, 0.0119 Hz and 0.346 Hz, respectively. Again, the operating wavelength of the radar was 24.9 meters. This gives a radial surface current away from the radar of 17.55 cm s^{-1}.

4   Conclusions and future recommendations

4.1   Conclusions

SuperDARN has always been able to detect sea scatter. However, until now, it has never been detected in a way that could glean useful information about the sea. With the advent of a new raw time series analysis (TMS), the detection of Bragg peaks and thus sea state has become possible. This study has proven, for the first time, that SuperDARN radars can detect useful information about sea state. In fact, with minor adjustments to the radar operating system and analysis techniques, it will be possible to produce wind-wave maps and calculate radial surface currents as a zero cost by-product of routine ionospheric research.

In Chapter 1, it was discussed how the scalar wave spectrum is related to wind velocity for fully developed seas. The scalar wave spectrum can be extracted from the second-order side bands located adjacent to the first-order Bragg peaks in the Doppler spectra. In Chapter 2, the variation of Bragg frequency with group path was investigated, and although the variation was significant, for most practical group paths the Bragg frequency was only slightly less than the Bragg frequency for surface mode propagation. In Chapter 3, the Bragg peaks were identified by applying a FFT to the raw time series of in-phase and quadrature amplitudes. From these spectra, wind directions were inferred by comparing the relative magnitudes of the advancing and receding Bragg peaks to a model directional wave spectrum. The method for determining radial surface current in the presence of an ionospheric Doppler shift was outlined; it simply involves measuring the shift of the ground scatter and Bragg peaks from their rest locations. Strictly, radial surface currents were not actually measured because Macquarie Island is presently outside the field of view of TIGER Tasmania. Only the *method* by which to calculate them was illustrated.

In summary, this thesis has pioneered the application of the SuperDARN radar network for oceanographic research.

4.2 Future recommendations

4.2.1 Wind-wave mapping

In Chapter 3.2.2 it was explained how to calculate the prevailing wind-wave direction with respect to the radar direction. This technique narrows the prevailing wind direction to one of two directions. By simply knowing whether the prevailing wind direction is toward or away from the second radar, the directional ambiguity is solved. The addition of another two Bragg peaks observed at a different angle also provides redundancy in the estimation of the actual wind direction. The phase velocity of the sea waves is controlled by the gravity wave dispersion relationship, equation (2.4). However, estimating the wind speed depends on observing well developed second-order Bragg peaks in the Doppler spectrum.

With suitable changes to the radar operating system and control programs, production of directional wind-wave maps for vast regions of the Southern Ocean will become possible. This will be a zero cost by-product of normal TIGER operation. Indeed, directional wind-wave maps can be produced by all SuperDARN radars with water bodies encompassed by their field of view. Moreover, this will not necessarily hamper the collection of valuable ionospheric data. In fact, it has the potential to enhance the collection of ionospheric data, for example, by improving the correct identification of ionospheric and sea scatter.

An ideal operating mode for a dedicated directional wind-wave experiment would be to run fast_scan_tms on all 16 beams, and to collect data at 70 range bins starting at 900 km and separated by 15 km. Using an effective integration time of 128 s, it would take approximately 34 minutes to record $16 \times 70 = 1120$ high resolution time series for subsequent Doppler analysis. A suitable day time operating frequency would be 12 MHz. However, in another mode, the frequency might be altered from one scan to the next to increase the area covered.

There are, however, some technical problems to be overcome. For example, ideally the radar operating system needs to be modified to permit 128-s integration times

(presently, there is a ~22 s limit). Also, an extensive collection of data analysis software needs to be written.

4.2.2   2D surface current measurements

With the addition of TIGER Unwin, 2-dimentional vector analysis of the ionospheric motion and ocean surface currents will become possible. Figure 4.1a shows the geometry of the problem when the line-of-sight Doppler velocities are at right angles to each other. Determining the speed and direction of the target, **v,** in this case is trivial. The vector **v** is simply the vector addition of the line-of-sight Doppler velocities, v_A and v_B.
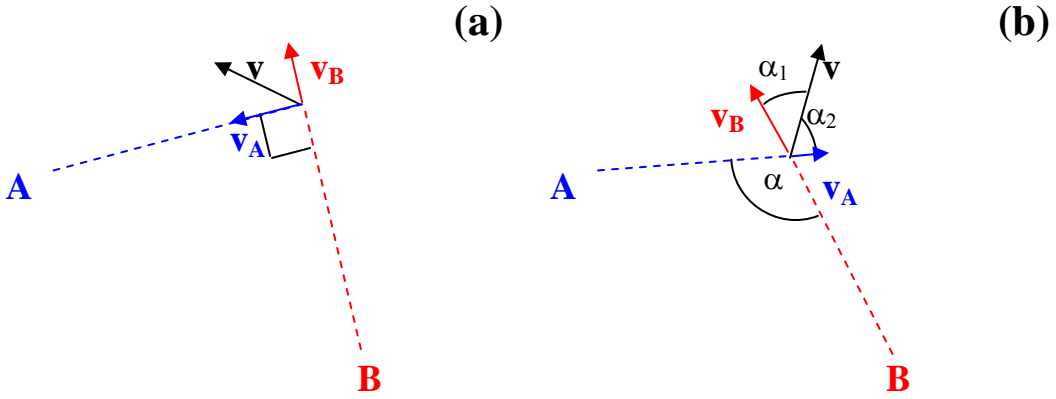

Figure 4.1: Vector diagrams showing line-of-sight Doppler velocities, v_A and v_B, of a surface current, **v** measured by two radars, A and B. In (a), v_A and v_B are at right angles, whereas in (b) they are separated by some angle α.

In the case illustrated by Figure 4.1b, the angle separating v_A and v_B has an arbitrary value, α. The solution of the absolute vector **v** is obtained as follows. The vector **v** can be described by the following relationships:

$$v_B = \mathbf{v}\cos(\alpha_1) \tag{4.1}$$

$$v_A = \mathbf{v}\cos(\alpha_2) \tag{4.2}$$

$$\alpha_1 + \alpha_2 = \alpha \tag{4.3}$$

where v_A, v_B, **v**, α, α_1, and α_2 are pictured in Figure 4.1b. From the geometry of the experiment and measurements, v_A, v_B and α are know, whereas **v**, α_1, and α_2 are the unknowns. By substituting equation (4.3) in equation (4.1) we reduce the problem to two equations with two unknowns:

$$v_B = \mathbf{v}\cos(\alpha - \alpha_2) \qquad (4.4)$$

$$v_A = \mathbf{v}\cos(\alpha_2) \qquad (4.5)$$

Cross multiplying equation (4.4) with equation (4.5) eliminates **v** and we obtain an equation with only one unknown:

$$v_B \cos(\alpha_2) = v_A \cos(\alpha - \alpha_2) \qquad (4.6)$$

Solving equation (4.6) for α_2 gives:

$$\alpha_2 = -\arctan\left(\frac{v_A \cos(\alpha) - v_B}{v_A \sin(\alpha)}\right) \qquad (4.7)$$

Substitution equation (4.7) into equation (4.2), and solving for **v** gives:

$$v = \frac{v_A}{\cos\left(-\arctan\left(\dfrac{v_A \cos(\alpha) - v_B}{v_A \sin(\alpha)}\right)\right)} \qquad (4.8)$$

Equation (4.8) simplifies to:

$$v = \frac{\sqrt{v_A{}^2 + v_B{}^2 - 2v_A v_B \cos(\alpha)}}{\sin(\alpha)} \qquad (4.9)$$

Hence the speed and direction of the surface current are given by equations (4.8) and (4.7), respectively. Equations (4.7) and (4.8) are valid for all azimuths of **v**.

Further improvements to the surface current measurements will involve the use of Macquarie Island. When both radars contain Macquarie Island in their fields of view, its Doppler signature can be used to subtract the Doppler shift due to ionospheric motion. Ground scatter would have a Doppler shift of zero Hz if it were not for the net vertical motion of the ionosphere throughout the integration period due to gravity waves and ULF waves. These ionospheric Doppler shifts will also average away to near zero over intervals greater than the diurnal tide. However, elimination of near real-time ionospheric Doppler shifts will be more successful for the northern hemisphere radars which have many artic islands in their fields of view.

There is the possibility that new current systems may be observed in the Southern Ocean. These currents may be essential to understanding changes in the world climate.

4.2.2 Additional applications for the TMS operating system

The applications for raw time series analysis are not limited to the measurement of sea state. As was previously stated, this approach was designed with the detection of meteor echoes in mind. This is because the use of long integration times could not resolve the rapid rise and slow decay of echoes characteristic of meteors. Other regions of interest for raw time series analysis include; the detection of icebergs, the detection of ships in the Southern Ocean, and mineral deposits in Antarctica.

Icebergs will usually not be detected by TIGER, as they are usually not present at ranges where most sea scatter is observed. Ocean currents usually do not transport icebergs equatorward of the Antarctic convergence, and even when they do, the icebergs will usually melt before drifting the ~1000–2000 km needed to be observed by the radar. Even so, other SuperDARN radars regularly observe the effects of ice in the field of view, usually in the form of reduced backscatter power [8] [26]. The effect of icebergs is to suppress ocean waves, and as such they can be detected by localised suppression of the Bragg peaks. Certainly if a transponder were placed on an icebergs, TIGER would be able to detect and track its movement.

The detection of ships using SuperDARN radars is also a possibility. The effective radar cross section of a ship is increased due to its conductive superstructure and wake. Aircraft carriers, for example, are capable of traveling at velocities up to 15 m s^{-1} or 35 knots. Therefore the Nyquist frequency needs to be adjusted to $\sim \pm 1.5$ Hz for operating frequencies of ~12 MHz. Figure 4.2 shows a real Doppler spectrum
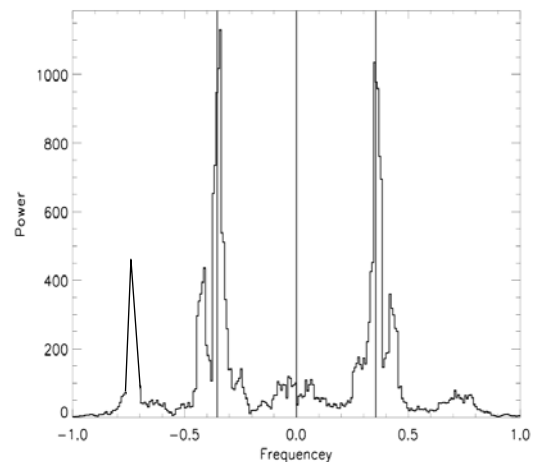

Figure 4.2: Imaginary ship echo superimposed on a real radar sea echo spectrum.

with an imaginary ship echo. If a spectrum like this were to be observed, it would suggest that a large ship moved towards the radar at ~9 m s^{-1}. If the same target were detected by TIGER Unwin, the speed and direction could be calculated.

The Aurora Australis is a 94.8 m long vessel used to supply bases in the Australian Antarctic Territories. Because the Aurora Australis has a cruising speed of 13 knots, we would expect to observe a sharp Doppler peak located at +0.54 Hz when it moved directly away from or towards the radar. The deployment of a transponder on the vessel would help validate the initial detection of the vessel. It would be interesting to see if the TIGER radar can be used to track the Aurora Australis en route to and from Antarctica during the summer.

The use of the raw time series analysis on the SuperDARN radars having fields of view located over the Antarctic ice shelf, such as the Sanae and Halley radars, would help improve the detection of minerals imbedded within the ice. The power of signals reflected from ice are weak compared to those reflected from the ground. The radio waves also penetrate the ice to some skin depth which increases with decreasing frequency. By using the superior Doppler resolution of the raw time series analysis, it should be possible to map the location and density of imbedded minerals with improved accuracy.

Bibliography

[1]   Lamb, H., *Hydrodynamics*. 6th ed. 1945, New York,: Dover Publications. 738.

[2]   Stewart, R.H., *Introduction To Physical Oceanography*. 2004: Texas A & M University. 312.

[3]   Pierson, W.J. and L. Moskowitz, *A proposed spectral form for fully developed wind seas based on the similarity theory of S.A. Kitaigordskii. J.* Geophysical Research Letters, 1964. **69**(5181–5190).

[4]   Watson, A. *The South Australian Wave Rider Buoy and Some Preliminary Comparisons of Wind and Wave Data. in Scientific and Technical Workshop XVII*. 2001. Perth, Western Australia.

[5]   Anderson, S.J., *Remote Sensing with the Jindalee Skywave radar.* IEEE Journal of Oceanic Engineering, 1986. **11**(2): p. 158 - 163.

[6]   Georges, T.M. and J.A. Harlan. *The Case for Building a Current-Mapping Over-the-horizon Radar. in IEEE Sixth Working Conference on Current Measurement*. 1999. San Diego, CA.

[7]   Parkinson, M.L., *Observations of the Broadening and Coherence of MF/lower HF Surface-Radar Ocean Echoes.* IEEE Journal of Oceanic Engineering, 1997. **22**(2): p. 347-363.

[8]   Kingsley, S.P., *The Coherence of H.F. Radar Sea Echoes.* GEC Journal of Research, 1986. **4**(03): p. 203-210.

[9]   Barrick, D.E., *Extraction of wave parameters from measured HF radar sea-echo Doppler spectra.* Radio Science, 1977. **12**: p. 415-424.

[10]   Baker, K.B., et al., *HF radar signatures of the cusp and low-latitude boundary layer.* J. Geophys. Res, 1995. **100**: p. 7671-7695.

[11]   Baker, K. *FITACF: A SuperDARN Tutorial. in Anual SuperDARN conference*. 2002. Valdez, Alaska.

[12]   Dyson, P.L. and J.C. Devlin. *The TIGER Radar - An Extension of SuperDARN to sub-auroral latitudes. in WARS'00 (Workshop on Applications of Radio Science) Proceedings*. 2000. La Trobe University.

[13]   Yukimatu, A.S. and M. Tsutsumi, *A new SuperDARN meteor wind measurement:Raw time series analysis method and its applications to mesopause region dynamics.* Geophysical Research Letters, 2002. **29**(20): p. **42** - 1 **42** - 4.

[14]   Yukimatu, A.S., et al., *A new method for monitoring and removing SuperDARN radar DC offsets.* Advances in Polar Upper Atmospere Research, 2002. **16**: p. 181-192.

[15]   Milan, S.E., et al., *Initial backscatter occurrence statistics from the CUTLASS HF radars.* Annales Geophysicae, 1997. **15**: p. 703 - 718.

[16]   Monselesan, D. and P. Wilkinson, *First step towards tiger frequency management: A ray tracing exploration using both IRI and IGRF models.* Advances in Space Research, 2001(1): p. 167-174.

[17]   Bennett, J.A., *The ray theory of Doppler frequency shifts.* Australian Journal of Physics, 1968. **21**: p. 259 - 272.

[18] Dyson, P.L., R.J. Norman, and M.L. Parkinson. *Ionospheric propagation modes identified using the TIGER HF radar*. in *The Workshop on the Applications of Radio Science*. 2002. Leura, Australia.

[19] Cochin, V., et al. *Anomaly detection in VHF radar measurements*. in *IGARSS*. 2004. Anchorage, Alaska Egan convention center.

[20] Pedrotti, F.L. and L.S. Pedrotti, *Introduction to optics*. 1993, 551 p.

[21] Parkinson, M.L., P.L. Dyson, and P.R. Smith, *Analysis of direction-of-arrival aliasing for MF/HF Doppler-sorted interferometry measurements of ionospheric drift*. Radio Science, 1997. **32**: p. 999 - 1009.

[22] Davies, K., *Ionospheric radio propagation*. 1965, xiv, 470 p.

[23] Yukimatu, S., *00Readme for new TMS version of RST/ROS V1.03*. 2003.

[24] Norman, R.J., M.L. Parkinson, and P.L. Dyson. *Comparing HF Radar Backscatter From the Southern Ocean With Ray-Tracing Results Using the IRI Model*. in *Workshop on the Applications of Radio Science*. 2004. Hobart, Tasmaina, Australia.

[25] Parkinson, M.L., *Advanced directional sea spectrum studies with the Bribie Island MF/lower HF surface-wave radar*. Radio Science, 1994. **29**(4): p. 815-830.

[26] Shand, B.A., et al., *CUTLASS HF radar observations of the Odden ice tongue*. Annales Geophysicae, 1998. **16**: p. 280-282.
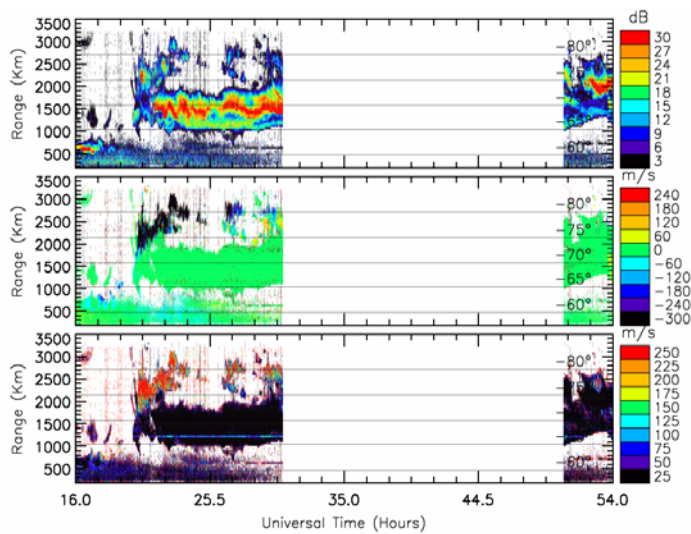
Appendix A

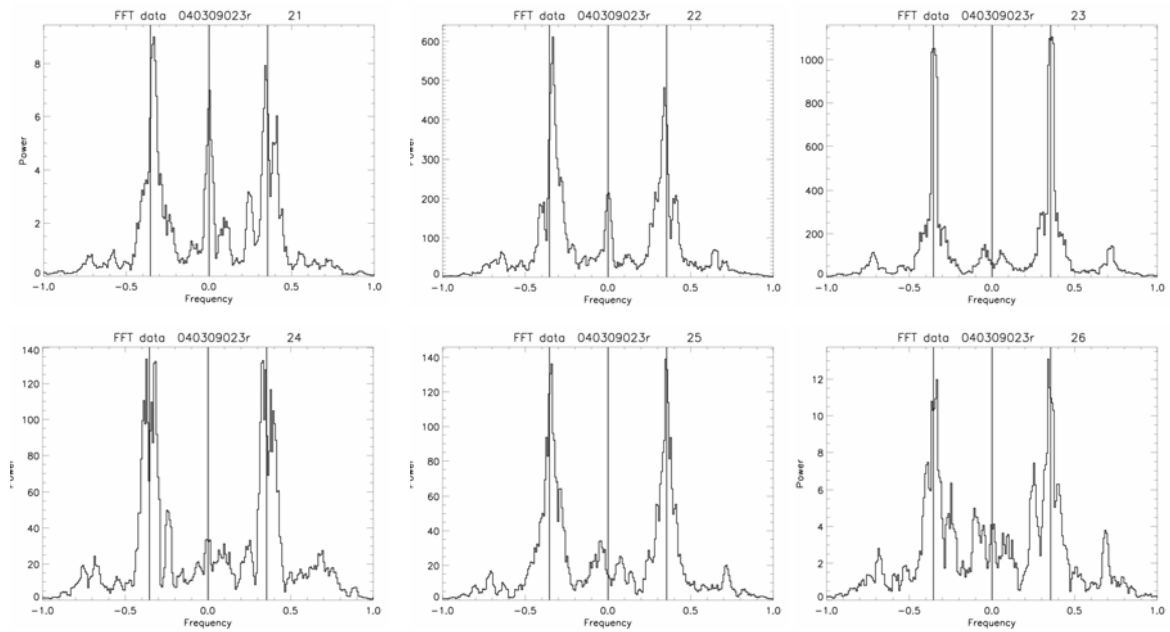### Summary plots of all three discretionary mode campaigns
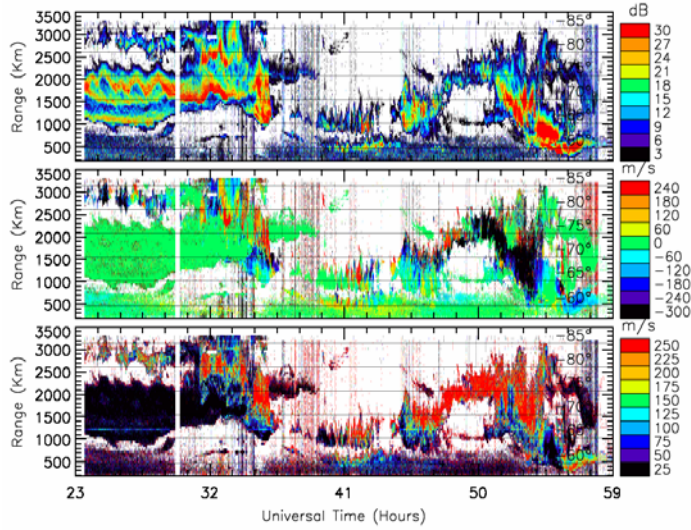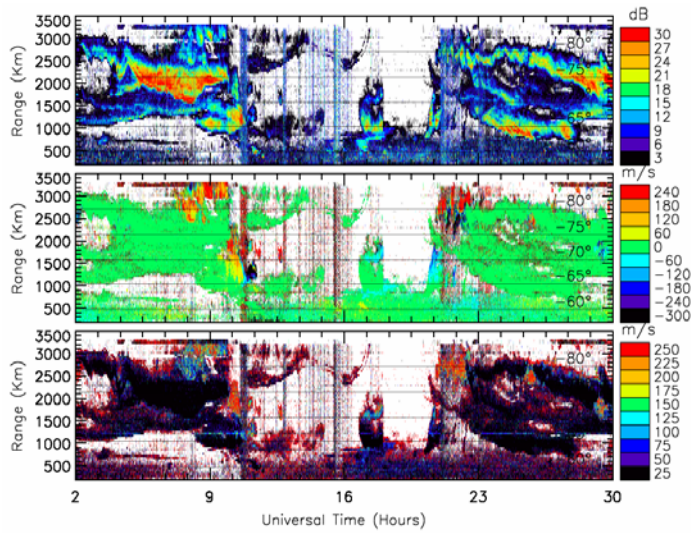
Appendix B

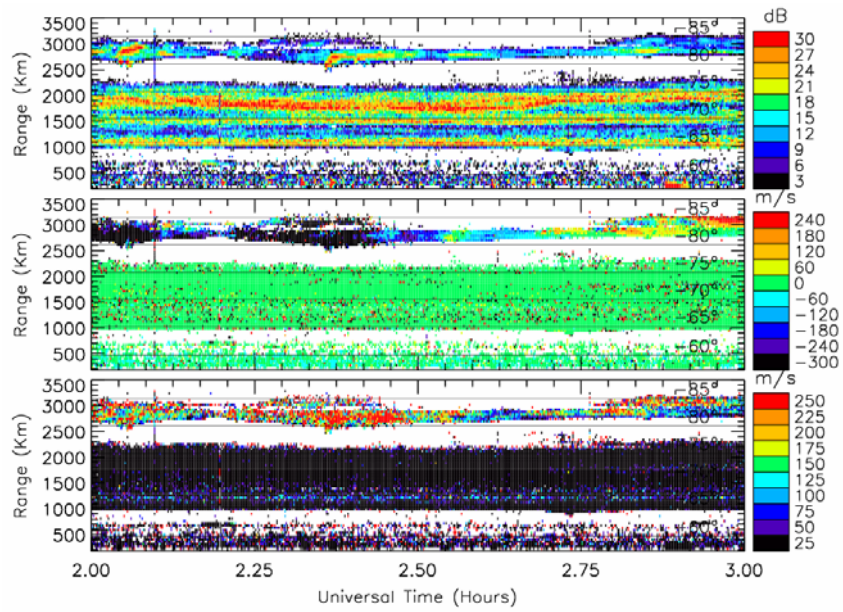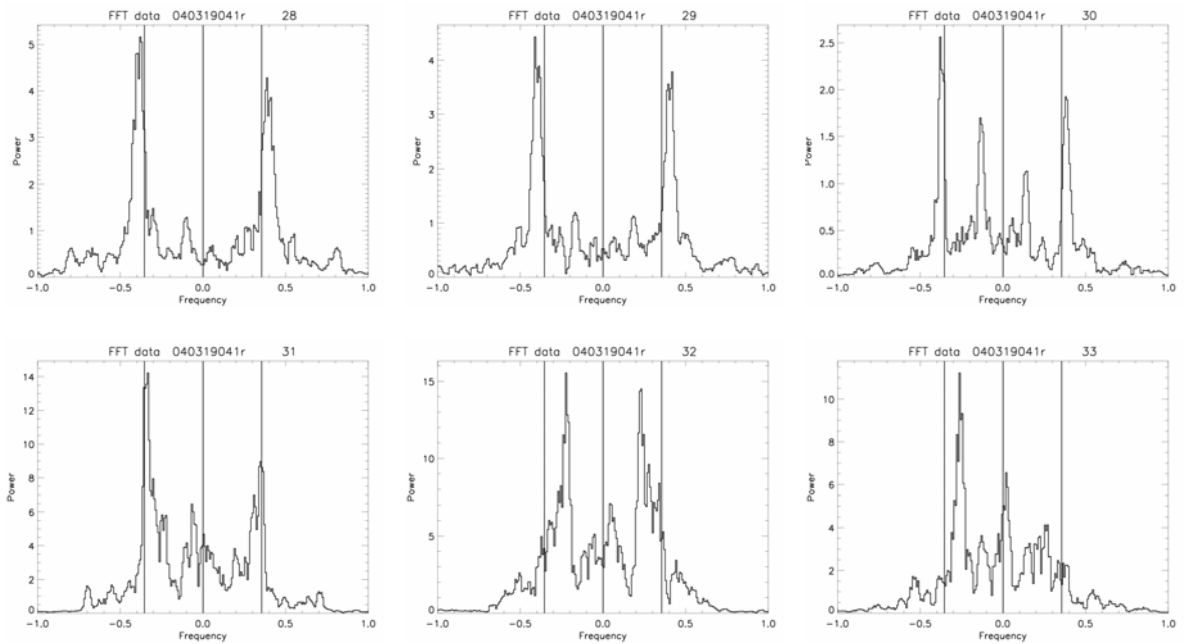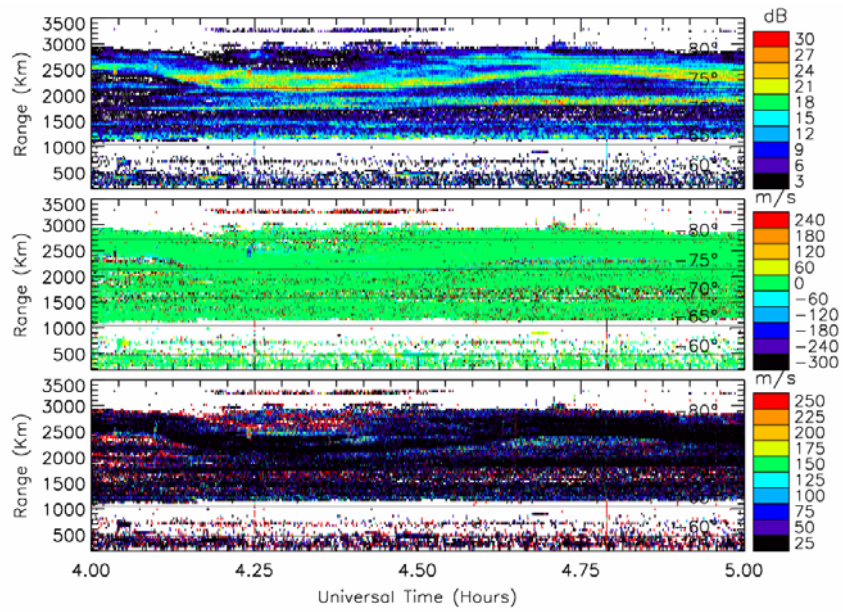## Reproducibility of Doppler spectra

Discretionary mode campaign A

Discretionary mode campaign B

Discretionary mode campaign C